# Short-Term Impacts of the Mega-Urbanizations of New Delhi and Los Angeles between 2000 and 2009

**Mark Z. Jacobson[1], Son V. Nghiem[2], Alessandro Sorichetta[3]**

[1]Department of Civil and Environmental Engineering, Stanford University, Stanford, California, U.S.A.

[2]Jet Propulsion Laboratory, California Institute of Technology, Pasadena, California, U.S.A.

[3]WorldPop, School of Geography and Environmental Science, University of Southampton, Southampton, U.K.

**Key Points:**

1) A new method of quantifying urban extent from satellite data is derived
2) New Delhi and Los Angeles urban extents increased ~80% and ~22.5% from 2000 to 2009
3) Such changes alone had substantial modeled impacts on short-term weather and pollution

**Abstract**

Urban areas are expanding worldwide due to increasing population, standard of living, and migration from rural areas. This study uses satellite and road data to quantify the urbanization of two megacities, New Delhi and Los Angeles, between 2000 and 2009. It then estimates, with a three-dimension nested global-through-urban climate, weather, and air pollution model, GATOR-GCMOM (Gas, Aerosol, Transport, Radiation, General Circulation, Mesoscale, and Ocean Model), the short-term atmospheric impacts of such urbanization alone. The simulations account for changes in meteorologically driven natural emissions, but not anthropogenic emissions, between 2000 and 2009. New Delhi's urban extent, defined based on the physical existence of its built structures and the transitional gradient from buildings to rural areas rather than on abrupt administrative borders, increased by ~80%, and Los Angeles', by ~22.5% between 2000 and 2009. New Delhi experienced a larger increase in its urban extent relative to its population during this period than did Los Angeles. In both megacities, urbanization increased surface roughness, increasing shearing stress and vertical turbulent kinetic energy, decreasing near surface and boundary layer wind speed, contributing to higher column pollution levels. Urbanization may also have increased downward solar plus thermal-infrared radiation fluxes to the ground and consequently upward latent and sensible heat fluxes from the ground to the air, increasing near-surface air temperatures. As such, urbanization alone may have had notable impacts on both meteorology and air quality.

## Plain Language Summary

This study quantifies, with satellite and road data, the changes in urban extent of two megacities between 2000 and 2009. During that period, the urban extent of New Delhi was found to have increased by ~80%, and that of Los Angeles', by ~22.5%. The study then estimates, with a three-dimension model nesting from the globe to each urban area, the short-term impacts of such urbanization alone. In both megacities, urbanization increased near-surface air temperatures and decreased wind speeds while increasing vertical turbulence and the column abundance of several pollutants due to the wind stagnation. As such, urbanization may impact both meteorology and air quality notably.

## 1. Introduction

Megacities worldwide are expanding rapidly [*Bagan and Yamagata*, 2014], changing the Earth's landscape and impacting local weather and climate. Two large megacities experiencing significant change are New Delhi and Los Angeles. This study uses a new remote sensing algorithm to quantify changes in the urban extents of New Delhi and Los Angeles from 2000 to 2009. It then uses the GATOR-GCMOM model described in Section 4 to assess the impacts of such changes, along with estimated changes in road coverage, on short-term weather and climate in each location. Results are compared with those from a related study for Beijing [*Jacobson et al*., 2015]. New Delhi and Los Angeles are chosen not only due to their different sizes and growth rates but also due to the fact that the former is inland while the latter is coastal. Thus, each is subject to different meteorological conditions. Both are subject to heavy anthropogenic air pollution.

The study period of 2000-2009 is examined because it is an important reference decade to investigate long-term urban changes and impacts, as it is the first decade of the new millennium during which extreme urbanization occurred in Asia (e.g., New Delhi) versus moderate changes elsewhere (e.g., Los Angeles). Moreover, the decade of the 2000s witnessed an abundance of well-calibrated new satellite observations and innovative methods, such as the one described herein, that enable new global capabilities to advance land-cover-land-use-change science.

Some previous studies have examined the expansion of urban infrastructure near or in New Delhi and Los Angeles. For example, *Rahman et al.* [2012] used remote sensing to find a five-fold increase in the urbanized area of the northwest district of Delhi from 1972-2003. *Sharma and Joshi* [2013] estimated an increase of 70.4 $km^2$ in a heavily built-up area of Delhi from 1998-2011 using Landsat satellite products. *Bagan and Yamagata* [2014] used Landsat data to detect an increase in the settlement area of Los Angeles city proper of 40% between 1986 and

2009. Nevertheless, a fundamental obstacle remains in distinguishing many impervious urban surfaces spectrally from pervious soils [*Weng et al*., 2009]. Accurate and repeatable quantification from spectral data, such as from Landsat, has also proven elusive [*Li et al*., 2014].

Urbanization impacts weather and climate in multiple ways. First, urban materials warm the surface through the Urban Heat Island (UHI) effect [e.g., *Howard*, 1833; *Oke*, 1982] by reducing evapotranspiration and changing the heat capacities, thermal conductivities, albedos, and emissivities of the surface. *Mohan et al.* [2013] and *Grover and Singh* [2015] have estimated the UHI effect in Delhi. *Vahmani and Ban-Weiss* [2016] have estimated it in Los Angeles.

Urban surfaces also affect wind speed, vertical turbulence, cloudiness, and precipitation by changing surface roughnesses, soil moisture, humidity, temperature gradients, and pressure gradients. *Lal and Pawar* [2011], for example, found an increase in rainfall and lightning between 2000 and 2008 over Delhi and attributed it to increased convective activity due to urbanization rather than changes in aerosol loading. *LaDochy and Witiw* [2012] associated the UHI effect in Los Angeles with a decrease in dense fog.

This study uses a technique not used in any previous study to calculate the urban extents of New Delhi and Los Angeles. This technique captures the gradient of the rural-urban transition rather than treating the transition as an abrupt binary boundary. It also captures moderate and some small towns not captured with the methodology described in *Jacobson et al.*, [2015]. An abrupt urban-rural boundary is physically unrealistic as the rural to urban change is a transitional gradient rather than an abrupt discontinuity. An abrupt change is a mathematically ill-posed problem that forces a singularity due to the unbounded derivative, potentially causing unrealistic features or increasing uncertainty in the numerical modeling. The new method, which derives gradual changes from satellite observations, represents realistically the gradual rural-urban

transition. It thereby overcomes the unrealistic, non-physical condition introduced by the abrupt boundary.

## 2. Determination of urban extent

Urban extent is generally defined as the spatial area of settlement of a population in an urban area. However, calculations of urban extent are performed differently and often arbitrarily within and among countries based on local administrative, political, or legislative decisions. Many definitions are non-physical and cannot be applied to three-dimensional climate-air quality models, which require a realistic representation of physical urban infrastructure and superstructures within it.

A usual method of quantifying urban extent is from optical or multi-spectral satellite remote sensing. Until recently, satellite remote sensing of land cover and land use change (LCLUC) had been limited to 2-D lateral coverage (latitude and longitude). Identifying and monitoring urban changes in 3-D (lateral and vertical expansion) have the potential to improve our understanding of LCLUC. To that end, the Dense Sampling Method (DSM) [*Nghiem et al*., 2009], which uses radar backscatter data acquired by a satellite conically-scanning scatterometer, was developed to measure urbanization in many parts of the world over a decadal time scale, thus in 4-D (3-D in space and 1-D in time).

By definition, a scatterometer is an accurate and stable radar. It enables the consistent monitoring of 3-D urban changes over time. With a wide swath (1400-1800 km), a scatterometer aboard a satellite in a low Earth orbit allows global observations of urban and rural transformations. Radar backscatter data represent urban observations on the basis of physical infrastructures (houses, buildings, factories, shopping centers, skyscrapers, freeway networks, etc.). This is because radar backscatter depends on the number of, size of, and materials within

buildings (e.g., higher backscatter for more buildings, for larger and taller buildings, and for stronger materials like steel) [*Jacobson et al*., 2015 and references therein].

In 2-D, the capability of DSM to delineate and monitor lateral urban changes has been validated against Percent Impervious Surface Area (%ISA) data from the National Land Cover dataset (which itself was independently generated from Landsat data) to characterize and quantify the expansion of major urban areas in the U.S. Great Plains [*Nguyen et al*., 2018]. Increases in DSM backscatter and %ISA between 2001 and 2006 agree with data in both magnitude and direction for multiple urban areas, including Omaha, Des Moines, Kansas City, Wichita, Tulsa, Oklahoma City, Dallas-Fort Worth, and Houston [*Nguyen et al*., 2018]. Previously, *Nghiem et al.* [2009] tested DSM in terms of geo-location, replication of the shape of the targeted area, and estimation of areal extent. DSM's accuracy was verified to within 4% for Príncipe Island, off the west coast of Africa in the Gulf of Guinea. *Jacobson et al*. [2015] found that DSM could delineate the 2-D urban extent of Beijing based on actual building structures in the urban built environment with an accuracy of 6% compared with independent observations from Landsat for the year 2000 and with an accuracy of 8% compared with the official urban extent for the year 2009.

The 3-D capability of DSM has been quantitatively demonstrated with 3-D airborne LIDAR-based estimations of building volume obtained from declassified U.S. Department of Defense data for several cities with different characteristics and socioeconomic conditions. For example, in Austin (Texas, U.S.), the 3-D fitting patterns characterizing the LIDAR 3-D building volume and the DSM backscatter are so similar that they are mostly indistinguishable (coefficient of determination $R^2 = 0.97$) [*Nghiem et al*., 2017]. From the DSM backscatter data, an empirical model function was derived to calculate building volume over the decade of the 2000s. The model found an increase of 9.3% in Austin's built-up area during the 2000s [*Nghiem*

128 *et al*., 2017]. DSM results for Almaty, Kazakhstan, a city with different superstructures from
129 Austin, Texas, indicate an astoundingly rapid 3-D building development rate of 70% per decade
130 in the urban core area, with an accuracy of 5% [*Groisman et al*., 2017].

131 Here, we apply DSM to determine 3-D changes in New Delhi (India) and Los Angeles
132 (California, United States). The mathematical formulation and verification of the DSM are
133 incorporated here by reference [*Nghiem et al*., 2009; *Nghiem et al*., 2014; *Groisman et al*., 2017;
134 *Nguyen et al*., 2018]. For this study, we use backscatter data collected from 2000 to 2009 by the
135 SeaWinds scatterometer aboard the QuikSCAT satellite [*QuikSCAT Mission*, 2014]. New Delhi
136 data are extracted from 27.0$^{o}$N to 30.0$^{o}$N latitude and from 75.0$^{o}$E to 79.5$^{o}$E longitude. Los
137 Angeles data are extracted from 32.0$^{o}$N to 35.0$^{o}$N latitude and 120.0$^{o}$W to 115.0$^{o}$W longitude. In
138 both regions, DSM backscatter ($\sigma_0$) and backscatter index of variability (backscatter IV) data are
139 produced with a regular grid resolution of 1/120$^{o}$ (0.00833$^{o}$) in both latitude and longitude,
140 which is equivalent to an equatorial posting pixel of approximately 1 km × 1 km. Figures S1 and
141 S2 show the resulting backscatter and backscatter IV in 2000 and 2009 for New Delhi and Los
142 Angeles, respectively.

143 Instead of using an approach that delineates the urban extent with an abrupt boundary, we
144 characterize the rural-urban transition with a combination of $\sigma_0$ and backscatter IV to capture
145 gradual changes from the natural rural environment to the urban built environment. Taking the
146 values of $\sigma_0$ and backscatter IV for the inner city (100% urban cover) and for the rural outskirt
147 (0% urban cover) as the training dataset, we determine the number of occurrences from a
148 minimum of 0 to a maximum of 10 when each pixel is determined as urban with different
149 combinations of $\sigma_0$ and backscatter IV thresholds. Specifically, this analysis tests combinations
150 of backscatter $\sigma_0$ from –7.8 to –9.6 dB in 0.2 dB increments (10 levels of $\sigma_0$) and backscatter IV

from 1.0 to 2.0 dB in 0.2 dB increments (6 levels of backscatter IV). The backscatter levels represent building volume change, transitioning as a gradient gradually from rural to urban areas. Backscatter IV levels identify human-made structures with azimuth alignment in contrast to random-azimuth objects in natural conditions (e.g., grasses, leaves, twigs, branches, etc.). The urban built environment is different between New Delhi and Los Angeles. As such, optimal backscatter IV values are determined separately for each study area to minimize errors, such as misidentifying urban areas as rural. For New Delhi, the optimal value of backscatter IV was found to be 1.8 dB. For Los Angeles, it was found to be 1.2 dB.

To avoid noisy results in the urban-rural classification, we select the number of occurrences greater than or equal to 2 (out of 10) for a pixel to be considered in the urban transition area going toward the urban core, which typically has a large count value. Moreover, we use the Shuttle Radar Topography Mission (SRTM) Water Body Dataset [*USGS,* 2018] to identify pixels containing surface water, such as over a river, lake, pond, reservoir, etc. Since the SRTM pixel is about 30 m compared with 1 km for DSM, we re-grid DSM results into the SRTM grid to determine the fractional urban versus water areas in the composite DSM-SRTM product. To do the re-gridding, we assign the DSM value in a given DSM pixel to each SRTM pixel whose centroid lies within the coarser DSM pixel. The fractional urban area in each DSM pixel is then calculated accounting for the number of SRTM water-body pixels (considered as non-urban) identified in each DSM pixel.

The composite product is then used to determine the urban fraction in each grid cell of the GATOR-GCMOM model used here to simulate the impacts of urbanization on New Delhi and Los Angeles over the decade of the 2000s. Some pixels at altitudes above 500 m were found to be misclassified as urban, mostly due to errors in mountains with steep slopes affecting both DSM backscatter and backscatter IV. These pixels were considered as non-urban in this study.

Figures 1a and 1c show the model domains used here of New Delhi and Los Angeles within India and California, respectively. Figures 2a and 2b show the New Delhi urban extents in 2000 and 2009, respectively, within the New Delhi model domain. Figures 3a and 3b show the same for Los Angeles. New Delhi's urban extent increased between 2000 and 2009 from 1834 $km^2$ to 3311 $km^2$, or by ~80.5%. Los Angeles' urban extent increased from 7120.4 $km^2$ to 8722.3 $km^2$, or by ~22.5%. The difference partly reflects the fact that the population of India grew by 15.3% (from 1.053 billion to 1.214 billion) between 2000 and 2009 [*World Bank*, 2018], whereas the population of the United States grew by only 8.7% (from 282.2 million to 306.8 million) during the same period [*U.S. Census Bureau*, 2018a]. The population of California similarly grew by 8.7% from 2000 to 2009. In both locations, the urbanization rate exceeded the population growth rate, but it did so more in India. One possible hypothesis for this, to be verified with future socioeconomic research beyond the scope of the study in this paper, is that the GDP (gross domestic product) per capita increased more percentage-wise in India (by 148%, from 439 to 1,090 USD) than in the United States (by 28.9%, from 36,450 to 47,002 USD) between 2000 and 2009 [*World Bank*, 2018]. This may have allowed a greater fraction of the India population to afford to build. An additional reason for the greater expansion of New Delhi may have been a greater migration from rural areas to cities, demanding more buildings for work and living, in India than in the United States.

## 3. Road surface area

The GATOR-GCMOM model treats roads, rooftops, and vegetated and bare soil surfaces at the sub-grid cell level [*Jacobson*, 2001a; *Jacobson and Ten Hoeve*, 2012]. However, urban extent data do not give a breakdown of how urban areas are divided into roads, rooftops, vegetation cover, and bare soil. Here, road surface areas in the New Delhi and Los Angeles urban extents

were estimated to improve the representation of surfaces in the GATOR-GCMOM model. The total road surface area within each pixel of each DSM-SRTM urban extent dataset in New Delhi was calculated using crowd sourced OpenStreetMap (OSM) road data [*OpenStreetMap,* 2018; *Jacobson et al., 2015*]. In Los Angeles, it was calculated using Topologically Integrated Geographic Encoding and Referencing (TIGER)/Line® road data [*U.S. Census Bureau,* 2018b].

OSM is a worldwide collaborative and voluntary effort to create and freely redistribute geospatial data. It represents the main, if not the only, source of road data in many countries [*Barrington-Leigh and Millard-Ball*, 2017]. Since 2010, several studies have assessed the quality of OSM road data, with results consistently indicating that both accuracy and completeness, although spatially heterogeneous, are generally good and significantly improving over time [*Haklay,* 2010*; Girres and Touya,* 2010; *Zielstra and Zipf,* 2010*; Zielstra and Hochmair,* 2011*; Koukoletsos et al.* 2012*; Neis et al.,* 2012*; Zielstra et al.,* 2013*; Wang et al.,* 2013*; Will,* 2014*; Zheng and Zheng,* 2014*; Forghani et al.,* 2014*; Siebritz,* 2014*; Zhao et al.,* 2015*; Molinari et al.,* 2016; *Brovelli et al.,* 2017; *Yagoub,* 2017*; Barrington-Leigh and Millard-*Ball, 2017; *Zhang and Malczewski,* 2018]. In particular, according to *Barrington-Leigh and Millard-Ball* [2017], OSM road data already cover about 83% of the global road network and almost 100% of the road networks in 77 countries, including in several low and middle-income countries.

The New Delhi OSM road data used for this study (Figure 1b) was downloaded from BBBike.org [*http://extract.bbbike.org/*] on March 18$^{th}$, 2016, and contains 23 types of roads that extend for a total length of about 77,517 km (*http://wiki.openstreetmap.org/wiki/Key:highway* provides a detailed description of the road types, which are listed in Table 1 for New Delhi).

The *U.S. Census Bureau* [2018b] TIGER database contains lines and polygons representing roads, water features, administrative and statistical boundaries, address information, and more [https://www.census.gov/geo/maps-data/data/tiger.html]. It was initially created to

facilitate and organize the 1990 Census [https://www.census.gov/newsroom/blogs/director/2014/11/happy-25th-anniversary-tiger.html]. The 2010 TIGER/Line® road data used here have an accuracy expectation of 7.6 m [*Zandbergen et al., 2011*] and a level of completeness reflecting the content of the US Census Bureau's Master Address File/TIGER database [*https://www.census.gov/geo/reference/gtc/gtc_maftiger.html*] on which all TIGER data are based. In 2011, after testing the accuracy of the 2010 TIGER road data, Los Angeles County used them as the basis for a new countywide address and street network file [*https://egis3.lacounty.gov/dataportal/2011/04/25/2010-tiger-roads/*]. The Los Angeles TIGER road dataset used here (Figure 1d) was extracted from the US Census Bureau's 2010 TIGER/Line Shapefiles: Roads [*https://www.census.gov/cgi-bin/geo/shapefiles/index.php?year=2010&layergroup=Roads*] and contains 13 types of roads that extend for a total length of ~190,924 km (*https://www.census.gov/geo/reference/mtfcc.html* provides a detailed description of the road types which are listed in Table 2 for Los Angeles).

The total road surface area in each pixel of the New Delhi and Los Angeles DSM-SRTM datasets in 2000 and 2009 is estimated as follows. First, the total length of each road type in each pixel is calculated after re-projecting the road vector data from Geographic Coordinate System (GCS) World Geodetic System (WGS) 84 to a customized WGS 84/Universal Transverse Mercator (UTM) Zone centered at 78° E longitude for New Delhi and to WGS 84/UTM Zone $11^{o}$ N for Los Angeles. Estimated road width means and standard errors for each road type in Tables 1 and 2 are taken from *Jacobson et al.* [2015], who calculated these statistics from 10 random samples of each road type in Beijing obtained from optical high-resolution images [*Google Earth Pro*, 2013]. Finally, the mean width of each road type is multiplied by the corresponding total road length in each pixel to obtain the surface area of each road type in each pixel. The sum over all road types represents the total road surface area in each pixel.

247 The total road surface area in each pixel in 2009 is simplistically assumed to be the same
248 as in 2016 for New Delhi (which uses 2016 OSM road data) and the same as in 2010 for Los
249 Angeles (which uses 2010 TIGER/Line® road data). The total road surface area in each pixel in
250 2000 is then estimated assuming that (1) all roads within the New Delhi and Los Angeles urban
251 areas in 2000 are the same as those in the 2000 urban area portion of the 2009 dataset, and (2)
252 only non-residential roads existing in 2009 outside of the 2000 New Delhi and Los Angeles
253 urban areas also existed in 2000. This latter assumption, which accounts for the fact that many
254 highways existing in 2009 pre-existed in 2000, may overestimate the total road surface area for
255 some road type in 2000 while underestimating total residential road areas.
256 The total road surface area in each pixel, determined from the road data, is then
257 interpolated into each corresponding GATOR-GCMOM grid cell. The total road surface area in a
258 given GATOR-GCMOM grid cell divided by the cell area represents the road fraction in the cell
259 (Figures 2 and 3). The maximum road fractions for New Delhi and Los Angeles in any cell were
260 35.8% and 31.2%, respectively. The total road surface areas in the New Delhi and Los Angeles
261 model domains in 2009 were 1123 $km^2$ and 2558 $km^2$, respectively. Thus, road areas represented
262 8.4% and 13.6% of the 2009 urban areas in New Delhi and Los Angeles, respectively.
263 Finally, the road surface area in each GATOR-GCMOM grid cell is subtracted from the
264 total urban area in the same grid cell, determined from the DSM-SRTM urban extent dataset, to
265 obtain the non-road urban area in each cell. All non-road urban areas in a GATOR-GCMOM
266 grid cell are assumed to consist of rooftops. Remaining areas in each grid cell are non-urban
267 areas, which are assumed to consist of either water, bare, or vegetated soil, with the vegetation
268 fraction derived from MODIS NDVI data as in *Jacobson and Ten Hoeve* [2012]. In the global
269 and coarsest model domains (Table 3), where DSM-SRTM urban extent data are not used, *USGS*

[2006] global land-use data at 0.01° resolution are used to determine land surface type. Such data include urban and build up land, agricultural land, and many types of natural lands.

## 4. Description of GATOR-GCMOM

The model used for this study is the global-through-urban nested climate-weather-air pollution model, GATOR-GCMOM (Gas, Aerosol, Transport, Radiation, General Circulation, Mesoscale, and Ocean Model), which is briefly described below [*Jacobson*, 2001a,b, 2012, 2014; *Jacobson et al*., 2007; *Jacobson and Ten Hoeve*, 2012]. GATOR-GCMOM simulates feedbacks among meteorology, solar and thermal-infrared radiation, gases, aerosol particles, cloud particles, oceans, sea ice, snow, roads, rooftops, soil, and vegetation without data assimilation or nudging. Model predictions have been compared with data in 19 peer-reviewed studies and have taken part in 11 multi-model inter-comparisons. In some of these studies, the model has been evaluated against paired-in-time-and-space gas, aerosol, radiative, and meteorological data in the Los Angeles Basin, itself (Jacobson et al., 1996, 1997, 2007). The last of these studies was a global-through-urban nested simulation with explicit treatment of 3-D clouds in the finest domain, just as in the present study. Figures 4 and S3 show additional comparisons of GATOR-GCMOM model results with Global Forecast Systems [*GFS*, 2018] reanalysis data for the India and California domains (defined in Table 3), averaged over January and July 2013. Considering that GFS assimilates observations for each reanalysis field, whereas GATOR-GCMOM does not, the similiarities in the spatial distribution of results are encouraging.

### Meteorological, Transport, Gas, and Surface Processes

On the global scale, the momentum equation is solved with the potential enstrophy, vorticity, energy, and mass-conserving scheme of *Arakawa and Lamb* [1981]. On regional scales, it is

294 solved with an enstrophy-, mass-, and kinetic-energy-conserving scheme [*Lu and Turco*, 1995].
295 Two-dimensional ocean mixed-layer dynamics conserve potential enstrophy, vorticity, energy,
296 and mass while providing mixed-layer velocities, heights, and energy transport [*Ketefian and*
297 *Jacobson*, 2009]. GATOR-GCMOM solves 3-D ocean energy and chemistry diffusion, 3-D
298 ocean equilibrium chemistry, and ocean-atmosphere exchange with mass conserving and
299 unconditionally stable schemes among 10 ocean layers [*Jacobson*, 2005].

300 Horizontal and vertical atmospheric advection of gases and size- and composition-
301 resolved aerosol particles are solved with the scheme of *Walcek* [2000]. Eddy diffusion
302 coefficients are calculated as in *Mellor and Yamada* [1982]. Gas processes include emissions,
303 photochemistry, gas-to-particle conversion, gas-to-cloud conversion, gas-cloud exchange, gas-
304 ocean exchange, advection, convection, molecular diffusion, turbulent diffusion, and dry
305 deposition. Gas photochemistry is solved with SMVGEAR II for over 400 tropospheric and
306 stratospheric kinetic, heterogeneous, and photolysis reactions.

307 In each land surface grid cell, the model treats water and energy transport through 10
308 subsurface soil layers for each of 13 subgrid soil types, if present. It also treats energy transfer
309 through roads or vegetation overlying soil; rooftop material; snow over roads, rooftops,
310 vegetation, and soil; water bodies; sea ice over water; and snow over sea ice over water
311 [*Jacobson*, 2001a; *Jacobson and Ten Hoeve*, 2012]. Energy transfer through and other impacts of
312 building walls were not treated as this would require characterization of wall size and type as
313 well as a more elaborate treatment of external versus internal temperatures modified by air
314 conditioning for cooling or heating, for which data were unavailable. The model further solves
315 for the depth, aging, compaction, and horizontal transport of sea ice while conserving mass
316 [*Jacobson and Ten Hoeve*, 2012; *Jacobson et al*., 2015].

317 Roads are assumed to consist of 5-cm-thick asphalt, impermeable to water and with
318 asphalt properties, overlying soil. In terms of the 10-layer subsurface module, the top five layers
319 are asphalt, and the rest, a soil-air-water mixture. Snow and liquid water can accumulate on the
320 asphalt as an additional ($11^{th}$) layer in the subsurface module. Roofs are assumed to consist of
321 five layers of roofing material on top of five layers of air [*Jacobson*, 2001a; *Jacobson and Ten*
322 *Hoeve*, 2012]. Dew that collects on the roof can evaporate.

323 During each 15 s subsurface module time step, surface and subsurface parameters are
324 calculated for each surface class in each grid cell from the column subsurface module. Surface
325 temperatures, sensible heat fluxes, latent heat fluxes, and water vapor fluxes are then weighted
326 by the fractional surface type in the cell to give an effective value for the whole cell. *Jacobson*
327 [2001a, Fig. 3 and 2001b, Fig. 3] compare modeled temperatures from this method with hourly
328 data over four days at two-dozen locations, including in cities.

329 The surface albedo of each grid cell for each wavelength is the area-weighted sum of the
330 albedos of each surface class in the cell. The albedos of roads and roofs are assumed to be those
331 of asphalt. Solar albedos of paved asphalt range from 0.04 (new) to 0.17 (aged), averaging 0.12
332 [*Pomerantz et al.,* 2000]. Albedos of all other surfaces are from $0.05^{o}$ resolution MODIS
333 combined Terra plus Aqua satellite data in seven spectral bands [*MODIS/USGS*, 2007; *Schaaf et*
334 *al.*, 2010]. These solar albedos are interpolated spatially and spectrally to each of 86 solar
335 wavelengths below 800 nm and 232 solar-IR wavelengths/probability intervals from 800-10,000
336 nm.

337

338 <u>Aerosol Processes</u>

339 Aerosol processes include anthropogenic and natural emissions, binary and ternary homogeneous
340 nucleation, condensation, dissolution, internal-particle chemical equilibrium, aerosol-aerosol

coagulation, aerosol-hydrometeor coagulation, sedimentation, dry deposition, and transport [*Jacobson*, 2002, 2003, 2012]. The model treats any number of discrete aerosol size distributions, each with any number of size bins and chemicals per bin. Particle number and mole concentrations of each chemical are tracked in each size bin. The components within each size bin of each aerosol size distribution are internally mixed in the bin but externally mixed from other bins and other size distributions. For this study, one aerosol size distribution with 14 size bins ranging from 2 nm to 50 μm diameter is used in each grid cell of each domain. Aerosol components in each size bin include black carbon (BC), tar balls, other primary organic carbon, secondary organic carbon, $H_2O$(aq), $H_2SO_4$(aq), $HSO_4^-$, $SO_4^{2-}$, $NO_3^-$, $Cl^-$, $H^+$, $NH_4^+$, $Na^+$, soil dust, pollen, spores, and bacteria.

Convective Cloud, Stratiform Cloud, Aerosol-Cloud Processes

For each simulation (New Delhi and Los Angeles), three nested domains are used (Table 3). For the global and coarsest nested domain in each simulation, convective clouds are treated at the subgrid scale (with multiple sub-grid cloud clouds per column) and stratus clouds are treated at the grid scale. Size- and composition-resolved aerosols and gases are transported vertically within each sub-grid cloud. Size- and composition-resolved cloud and precipitation particles then form on top of the aerosol size distributions accounting for multiple microphysical processes [*Jacobson*, 2003; 2012; *Jacobson et al*., 2007]. For the innermost nested domain in each simulation, all cloud thermodynamics and microphysics are treated explicitly at the grid scale. Size- and composition-resolved cloud and precipitation particles form from size- and composition-resolved aerosol particles, and the cloud particles and their components are transported along with gases both horizontally and vertically [*Jacobson et al*., 2007]. In other words, clouds form and evolve in three dimensions in the innermost domain. On all scales, the

365 model treats three hydrometeor size distributions (liquid, ice, graupel), each with 30 size bins
366 (0.5 μm to 8 mm in diameter), and tracks concentrations of all aerosol component inclusions in
367 each size bin of each hydrometeor distribution.
368
369 Radiative Processes
370 For radiative calculations, each model column is divided into clear- and cloudy-sky columns, and
371 separate calculations are performed for each. Radiative transfer is solved simultaneously through
372 multiple layers of air and one snow, sea ice, or ocean water layer at the bottom to calculate,
373 rather than prescribe, spectral albedos over these surfaces. For vegetated or bare land surfaces,
374 no such layer is added. The 2-stream radiative code [*Toon et al., 1989*] solves the atmospheric
375 radiative transfer equation for radiances, irradiances, photosynthetically active radiation (PAR),
376 actinic fluxes, and atmospheric heating rates through each model layer in each column, over each
377 of 694 wavelengths/probability intervals in the ultraviolet, visible, solar-infrared, and thermal-
378 infrared spectra, accounting for gas and size- and composition-dependent aerosol and cloud
379 optical properties [*Jacobson*, 2012]. The intervals include 86 ultraviolet and visible wave
380 intervals from 170 to 800 nm, 232 visible, solar-infrared, and thermal-infrared probability
381 intervals from 800 nm to 10 μm, and 376 thermal-infrared probability intervals from 10 μm to
382 1000 μm. Solar radiation calculations are performed from 170 nm to 10 μm.
383 The model accounts for atmospheric scattering and absorption by gases and size- and
384 composition-resolved aerosol and hydrometeor particles. Since the model treats the time-
385 dependent evolution of the size and composition of aerosol particles and clouds and the
386 feedbacks of aerosol particles to atmospheric stability and winds, it accounts for the first indirect
387 effect, second indirect effect, and the semi-direct effect of aerosol particles on clouds.

Aerosol and cloud optical properties are calculated by integrating spectral optical properties over all size bins of each aerosol and hydrometeor particle size distribution. Aerosol spectral optical properties of a given size are determined by assuming that black carbon, if present, is a core surrounded by a mixed shell and that the aerosol liquid water content is a function of the ambient relative humidity and aerosol composition. Spectral scattering and absorption properties of aerosol particles within clouds but between cloud particles are determined based on an aerosol liquid water content determined at the relative humidity of the cloud. Cloud drop, ice crystal, and graupel optical properties are determined accounting for the time-dependent evolution of black carbon, brown carbon, and soil dust inclusions within them. As such, the model accounts for cloud absorption effects I and II, which are the heating of a cloud due to solar absorption by absorbing inclusions in cloud drops and by swollen absorbing aerosol particles interstitially between cloud drops, respectively [*Jacobson*, 2012].

Since the model tracks BC, tar balls, soil dust, and all other aerosol inclusions within precipitation particles that fall onto snow and sea ice, the radiative transfer calculation accounts for the optics of all these absorbing aerosol constituents within and between snow and sea ice grains [*Jacobson*, 2012].

Emissions

The anthropogenic emission inventory used for the global, India, and New Delhi domains (Table 3) is the Fifth Assessment Report (AR5) inventory for 2005 assuming the Representative Concentration Pathway (RCP) 4.5 trajectory [*Clarke et al.,* 2007]. This inventory is at 0.5-degree horizontal resolution. Emitted pollutants include CO, $CH_4$, acids, alcohols, benzene, butanes, chlorinated hydrocarbons, esters, ethane, ethene, ethers, ethyne, formaldehyde, hexanes and higher alkanes, ketones, other volatile organic compounds (VOCs), other alkanals, other alkenes,

412 other aromatics, pentanes, propane, propene, terpenes, toluene, trimethylbenzenes, xylene, NO,
413 $NO_2$, $NH_3$, $SO_2$, $SO_3$, BC, and primary organic carbon (POC). For $CO_2$, $N_2O$, CFCs, and HFCs,
414 the EDGAR 2005 inventory is used [*European Commission*, 2014].

415 The anthropogenic emission inventory used for the California and Los Angeles domains
416 is the U.S. National Emission Inventory (NEI) for 2008 [*USEPA*, 2010]. From the point, onroad
417 mobile, non-road mobile, and area source raw emission data, diurnally varying gridded
418 inventories are prepared at the horizontal resolution of each model domain.

419 For all domains, emissions of all components from open biomass and biofuel burning are
420 described in *Jacobson* [2014] as are heat and moisture fluxes from fossil fuel, biomass, and
421 biofuel combustion. Natural emissions from lightning (NO, $NO_2$, HONO, $HNO_3$, $N_2O$, $H_2O_2$,
422 $HO_2$, CO), soils (dust, bacteria, NO, $N_2O$, $H_2$, $CH_4$, $H_2S$, dimethylsulfide or DMS, OCS, CS),
423 oceans (bacteria, sea spray, DMS, $N_2O$, $H_2$, $CH_4$, $CH_3Cl$), and vegetation (pollen, spores,
424 isoprene, monoterpenes, methanol, other VOCs) are calculated as a function of modeled
425 meteorology as in *Jacobson and Streets* [2009].

426

427 **5. Simulations**

428 Eight global-through-urban nested simulations are performed, four for New Delhi (Case 1) and
429 four for Los Angeles (Case 2). Each simulation includes three nested domains – a global domain,
430 a coarse nested domain, and a fine (innermost) nested domain. Table 3 gives the locations and
431 resolutions of each domain for Cases 1 and 2. Vertically, the global domain has 68 sigma-
432 pressure layers from the ground to 0.219 hPa (≈60 km), including 15 layers in the bottom 1 km
433 and 500-m resolution from 1-21 km. All nested domains have 55 layers from the surface to 47.3
434 hPa, matching exactly the bottom 55 sigma-pressure levels of the 68-layer global domain.
435 Emissions enter all three domains, and all gas, aerosol, radiative, dynamical, and surface

processes are solved in all domains. Gas concentrations, size- and composition-resolved aerosol mole and number concentrations, temperature, specific humidity, and wind are transported one way from coarser domains to finer domains, allowing for long-range transport of pollutants into finer domains. Clouds are not transported from coarser to finer domains, but the liquid and ice water from clouds in coarser domains is evaporated/sublimated and the resulting latent heat used for evaporation/sublimation is removed from the air to conserve energy. The supersaturated water vapor and the cooler air are then transported to finer domains, where the water vapor can re-condense or re-deposit to form clouds and release its latent heat back to the air in the finer domains, thus conserving vapor and energy.

A five-row buffer layer at each horizontal boundary in each fine domain is used to relax concentrations and other variables to avoid spurious jolts at the boundaries [*Jacobson et al*., 2007].

The four simulations in each case include two for January and two for July. Each January simulation for a case is exactly identical to the other January simulation for the same case with respect to all results in both the global and coarse nested domains. However, in the innermost domain, one January simulation includes 2009 urban extent and roads and the other, 2000 urban extent and roads (Figures 2 and 3). The same applies to each pair of July simulations. Upon completion, differences from the innermost domain are taken between the January 2009 and 2000 simulations and between the July 2009 and 2000 simulations to estimate the impacts on short-term climate, weather, and atmospheric composition of changes in urban extent and roads alone in and around each megacity.

Meteorological fields in all domains are initialized with Global Forecast System $0.5^{o}$x$0.5^{o}$ reanalysis fields [*GFS*, 2018] on either January 1 or July 1 of an arbitrary common year, 2013,

460 when there was neither an El Niño nor a La Niña year (Null, 2018). These initial meteorological
461 fields are used for both 2009 and 2000 to ensure all differences between simulations in the
462 innermost domain are due to changes in urban extent and roads only and not initial
463 meteorological conditions.

464 Urban extent affects the areas of rooftops, roads, and other impervious surfaces. When a
465 roof or road land use type replaces a vegetated or unvegetated soil land use type in the model,
466 several surface properties change as well. First, when a road replaces soil or vegetated soil, water
467 can no longer evaporate from the soil below the road, but dew or rain can collect on the road and
468 that water can evaporate or drain to nearby creeks and rivers. Similarly, soil water cannot
469 evaporate when a building with a roof replaces soil or vegetated soil. Second, the heights;
470 surface roughness lengths for momentum, heat, and moisture; albedos; emissivities; thermal
471 conductivities; specific heats; and bulk densities of roads and roofs differ from those of vegetated
472 or unvegetated soil in the model [Section 3 and *Jacobson*, 2001a; *Jacobson and Ten Hoeve*,
473 2012].

474

475 **6. Results**

476 Figures 5-10 and Tables 4-5 summarize the relevant results of this study. Figures 5, 7, and 8 and
477 Table 4 illustrate the impacts of 2009 versus 2000 urban extent and roads for the innermost
478 nested domain of the New Delhi simulations. Figures 6, 9, and 10 and Table 5 show the same for
479 the Los Angeles simulations.

480 In both megacities, urbanization increased surface roughness lengths noticably in
481 locations where urban extent inreased (Figs. 5a, 6a). Greater surface roughness increased near-
482 surface shearing stress (Figs. 5b, 6b), increasing shear-driven eddies, increasing near-surface
483 vertical turbulent kinetic energy (TKE) (Figs. 5c, 6c). Vertical TKE is the mean kinetic energy

per unit mass associated with the vertical component of eddies in turbulent flow. TKE increases subsided with increasing altitude (Figs. 7a, 10a). Increases in TKE decreased near surface wind speeds (Figs. 5d, 6d) and, to a lesser extent, 100-m wind speeds (Tables 4-5; Figs. 7b, 10b).

Covering soil with impervious urban materials also reduced transfer of water from air to the soil and prevented precipitation from falling directly on soil, decreasing soil moisture in the locations where urban surfaces were added (Figs. 5e, 6e). Precipitation in the model either flowed to waterways or accumulated on impervious surfaces until it evaporated. Although urban surfaces also reduced evaporation of soil water to the air above the soil, allowing existing moisture to be retained better, the lack of moisture transfer and precipitation to the soil resulted in a net reduction in moisture under impervious surfaces. This factor, along with the increase in vertical TKE, which transported surface water vapor aloft, reduced near-surface water vapor mixing ratios over the areas of urbanization (Figs. 5f, 6f). Lower near-surface water vapor together with increases in near-surface air temperature due to urbanization (Figs. 5g, 6g), decreased near-surface relative humidity (Figs. 5h, 6h).

Near surface air temperatures increased over newly-urbanized land during both January and July in New Delhi and Los Angeles (Figs. 5g, 6g), consistent with many UHI studies, which are based on air temperature differences, usually between urban and rural locations. Changes in ground temperature over those same locations were more ambiguous (Figs. 5i, 6i). During January in New Delhi, for example, ground temperatures over the newly urbanized region slightly decreased on average (Fig. 5i), whereas in July, they increased in half the newly-urbanized region but decreased in the other half. It is generally known that the UHI effect is stronger in summer than in winter and that during the winter, urbanization can cause cooling during later hours of the night [e.g., *Chow and Bohumil*, 2011]. It is also known that vegetation in urban regions dampens the UHI [e.g., *Edmondson et al*., 2016] Based on an analysis of the

508 modeled parameters, the reason for the modeled winter ground cooling but air warming in New
509 Delhi was as follows. Ground temperature depends on a balance among the ground-to-air latent
510 heat flux, ground-to-air sensible heat flux, net downward minus upward solar plus thermal-
511 infrared radiation, and the conductive heat flux between the ground and layers of soil below the
512 ground [e.g., *Jacobson*, 2001b, Equation 8]. The increase in vertical TKE due to urbanization
513 (Figs. 5c, 6c) increased upward latent heat fluxes (Figs. 5j, 6j; Tables 4-5) and sensible heat
514 fluxes (Figs. 5k, 6k; Tables 4-5) in all cases. The reduction in albedo over urbanized areas (Figs.
515 5l, 6l; Tables 4-5) increased the net downward minus upward solar plus TIR radiation (Figs. 5m,
516 6m; Tables 4-5).

517 In the case of New Delhi in January, these three factors alone were enough to reduce
518 ground temperature (but increase air temperature) between 2000 and 2009. For example, the sum
519 of the upward latent and sensible heat fluxes minus the downard solar plus TIR resulted in a net
520 upward domain- and montly-averaged flux of 0.29 $W/m^2$ (Table 4). This net upward flux
521 transferred heat from the ground to the air above it, cooling the ground slightly and warming the
522 air.

523 In the case of Los Angeles in January, the domain-averaged ground temperature slightly
524 increased between 2000 and 2009 but the sum of the latent, sensible, and radiative heat fluxes
525 was net upward as well, 0.29 $W/m^2$ (Table 5). An increase in ground temperature together with
526 an increase in upward net energy flux was possible because the soil moisture under urbanized
527 land decreased in all cases (Figs. 5e, 6e), decreasing the thermal conductivity of the soil-water-
528 air mixture because the thermal conductivity of air is less than that of the water it replaces when
529 soil dries. The decrease in soil-water-air thermal conductivity between 2000 and 2009 decreased
530 the downward transfer of heat in January in Los Angeles, allowing the urbanized ground
531 temperature to increase slightly on average between 2000 and 2009.

For all simulations, no changes in anthropogenic emissions were assumed between 2000 and 2009. However, changes in meteorological conditions due to changes in urban surfaces affected natural emissions, such as sea spray, soil dust, pollen, spores, bacteria, natural biogenic gases, and lightning gases. For example, between 2000 and 2009 natural emissions in the innermost New Delhi domain changed as follows in the July average: soil dust, -30%; land spores, -1.5%; isoprene from vegetation, -0.74%; and soil $H_2S$, -1.1%; among other parameters. In the innermost Los Angeles domain, emissions changed as follows in the January average: soil dust, -3%; land spores, -3.7%; isoprene from vegetation, -0.69%; and soil $H_2S$, -4.6%; among other parameters. The land-based emissions decreased primiarly due to the fact that less land was available for natural emissions to occur over. They also changed due to changes in soil moisture, soil temperature, and wind speed.

The main meteorological impacts of urban surfaces are due to increases in vertical TKE and decreases in horizontal wind speed. Increases in TKE tend to reduce pollutant concentrations near the surface and increase them aloft. Decreases in wind speed tend to increase pollutant concentrations near the surface and aloft by decreasing advection of the pollutants out of the airshed. Temperature and water vapor also have impacts. Increases in temperature increase the rate at which ozone forms in polluted air but not in clean air, because higher temperature increases thermal dissociation of peroxyacetyl nitrate (PAN) and other nitrated organics, increasing organic radicals and the $NO_2$:NO ratio, both of which increase ozone [*Jacobson*, 2008]. Under high $NO_x$ conditions (such as in most urban airsheds), increases in $H_2O$ also increase ozone. The reason is that increases in $H_2O$ increase OH by $H_2O+O(^1D)\rightarrow 2OH$. OH then converts to $HO_2$ by a variety of reactions. Subsequently, $NO+HO_2\rightarrow NO_2+OH$ increases the $NO_2$:NO ratio, increasing ozone [*Jacobson*, 2008].

For both New Delhi and Los Angeles for both January and July, urbanization between 2000 and 2009 increased domain-averaged near-surface ozone (Figs. 5n, 6n; Tables 4-5) and ozone aloft throughout the boundary layer (Figs. 7f-10f). Higher air temperatures throughout the boundary layer in most cases (Figs. 7d-10d) contibuted as did the slower wind speeds throughout the boundary layer (Figs. 7b-10b). Near surface water vapor decreased, but elevated water vapor increased in most cases (Figs. 7c-10c) due to turbulent convection of surface water vapor to aloft. Higher water vapor aloft likely contributed to some increases in ozone there.

Anthropogenic black carbon aerosol emissions were held constant between 2000 and 2009 in all simulations, but BC column abundance increased in most simulations (Tables 4-5; Figs. 7g-10g) between 2000 and 2009 primarily because of the decrease in wind speed that reduced advection of BC out the innermost nested model domain. The increase in vertical TKE in all cases mixed some of the BC vertically, reducing surface concentrations in some cases (Figs. 5o, 6o; Tables 4-5). Aerosol optical depth similarly increased in many layers in most simulations (Figs. 7g-10g) since other aerosol constituents behaved similarly to BC.

Clouds are affected significantly by the relative humidity (which itself depends on water vapor and temperature) and the presence of cloud condensation nuclei. Water vapor (Figs. 7c-10c) and the relative humidity (Figs. 7e-10e) tended to decrease near the surface but increase aloft in most simulations. This resulted in slight decreases in surface fog but increases in cloudiness aloft. Precipitation decreased during January and July over the New Delhi domain but increased during both months over the Los Angeles domain (Tables 4-5).

Some difference plots (e.g., Figs. 5h, 5i, 5j, 5n, 6f, 6h, 6j in July) show changes near the surface outside of an urban region with magnitudes larger than those found inside the urban region. Such changes are physical and due to perturbations that propagate upward from the urban region, then horizontally away from the urban region, then downward to the surface. For

example, if the ground heats due to the addition of an urban surface, air rises and diverges aloft, decreasing the surface pressure over the urban area but increasing it away from it. Where the pressure increases most depends on wind direction and speed aloft. The wind aloft move the air some distance to a convergence region aloft, where the convergence with winds from another direction forces some air to descend, compress, and warm, increasing the surface air temperature and pressure (since convergence aloft exceeds divergence at the surface) far from the urban area. Other parameters are subsequently affected by these changes as well.

The feedbacks found here for New Delhi and Los Angeles outside of the urbanization region were in several cases greater than for Beijing, although the characteristics of results here are generally consistent with those for Beijing from *Jacobson et al*. [2015]. In that study, the impacts of a much larger relative increase in urban extent, 275% between 2000 and 2009, were modeled. There, it was similarly found that urbanization increased surface roughness, shearing stress, and TKE, decreasing near surface wind speed. It was also found that urbanization decreased soil moisture, surface albedo, surface water vapor, and surface relative humidity but increased near-surface air temperature and ozone. Thus, the results found here seem robust across three diverse geographies.

## 7. Summary and conclusions

This study used satellite and road data to estimate the urban extent and road networks of two megacities, New Delhi and Los Angeles, in 2000 and 2009. It then used the 3-D nested global-through-urban climate, weather, and air pollution model, GATOR-GCMOM, to quantify the short-term impacts of such urbanization alone on weather, climate, and air quality. The simulations accounted for changes, between 2000 and 2009, in meteorologically driven natural emissions, but not anthropogenic emissions. New Delhi's urban extent increased by ~80% and

Los Angeles', by ~22.5% between 2000 and 2009. The larger increase in New Delhi's urban extent relative to its population growth may be due in part to the greater relative increase in gross domestic product per capita of 148% in India versus the 28.9% in the United States during that period, although this was not proven here. In both megacities, urbanization may have increased surface roughness, shearing stress, and vertical turbulent kinetic energy, decreasing near surface and boundary layer wind speed, contributing to higher column pollution levels. Urbanization may also have increased downward solar plus thermal-infrared radiation fluxes to the ground and consequently upward latent and sensible heat fluxes from the ground to the air, increasing near-surface air temperatures. As such, urbanization alone had notable impacts on both meteorology and air quality.

**Acknowledgments**

This project received funding from the NASA SMD Earth Sciences Division and computer support from the NASA high-end computing center. The research carried out at the Jet Propulsion Laboratory, California Institute of Technology, was supported by the NASA Land-Cover and Land-Use Change (LCLUC) Program. The research carried out at the School of Geography and Environmental Science, University of Southampton, was done in the framework of the WorldPop Program (www.worldpop.org). The National Science Foundation (AGS-1441062) and the Stanford Woods Institute for the Environment additionally supported the research at Stanford. All input data used are listed in the text, tables, and references. Output data are provided in the tables and figures.

**References**

626 Arakawa, A., and V. R. Lamb (1981), A potential enstrophy and energy conserving scheme for
627 the shallow water equations, *Mon. Wea. Rev., 109*, 18-36.
628 Bagan, H., and Y. Yamagata (2014), Land-cover change analysis in 50 global cities by using a
629 combination of Landsat data and analysis of grid cells, *Environ. Res. Lett., 9*, 064015.
630 Barrington-Leigh C., and A. Millard-Ball (2017), The world's user-generated road map is more
631 than 80% complete, *PLoS ONE, 12*, e0180698. https://doi.org/10.1371/journal.pone.0180698
632 Brovelli, M.A., M. Minghini, M. Molinari, and P. Mooney (2017), Towards an automated
633 comparison of OpenStreetMap with authoritative road datasets, *Transactions in GIS*, *21*, 191-
634 206.
635 Chow, W.T.L., and M.S. Bohumil (2011), Analyses of nocturnal temperature cooling-rate
636 response to historical local-scale urban land use/land cover change, *J. Appl. Met. &*
637 *Climatology, 50*, 1872-1882.
638 Clarke, L., J. Edmonds, H. Jacoby, H. Pitcher, J. Reilly, and R. Richels (2007), Scenarios of
639 Greenhouse Gas Emissions and Atmospheric Concentrations, Sub-report 2.1A of Synthesis
640 and Assessment Product 2.1 by the U.S. Climate Change Science Program and the
641 Subcommittee on Global Change Research, 154 pp., Department of Energy, Office of
642 Biological & Environmental Research, Washington, D. C., USA,
643 http://tntcat.iiasa.ac.at:8787/RcpDb/dsd?Action=htmlpage&page=compare (accessed April 1,
644 2018).
645 Edmondson, J.L., I. Stott, Z.G. Davies, K.J. Gaston, and J.R. Leake (2016) Soil surface
646 temperatures reveal moderation of the urban heat island effect by trees and shrubs, *Scientific*
647 *Reports, 6*, 33708.

European Commission Joint Research Centre (JRC)/Netherlands Environmental Assessment Agency (PBL) (2014), Emission Database for Global Atmospheric Research (EDGAR), http://edgar.jrc.ec.europa.eu (accessed April 1, 2018).

Forghani, M., and M.R. Delavar (2014), A quality study of the OpenStreetMap dataset for Tehran, *ISPRS International Journal of Geo-Information*, *3*, 750-763.

GFS (Global Forecast System) (2018), $0.5^{o}$ x $0.5^{o}$ reanalysis fields, https://www.ncdc.noaa.gov/data-access/model-data/model-datasets/global-forcast-system-gfs (accessed September 27, 2018).

Girres, J. F., and G. Touya (2010), Quality assessment of the French OpenStreetMap dataset, *Trans. GIS, 14*, 435–459.

Google Earth Pro 7.1.2.2041 (2013), https://www.techworld.com/download/system-desktop-tools/google-earth-pro-7122041-3330263/ (accessed April 1, 2018).

Groisman, P. and 28 others (2017), Northern Eurasia Future Initiative (NEFI): facing the challenges and pathways of global change in the twenty-first century, *Progress in Earth and Planetary Science*, *4*, *41*. doi:10.1186/s40645-017-0154-5

Grover, A., and R.B. Singh (2015), Analysis of urban heat island (UHI) in relation to normalized difference vegetation index (NDVI): A comparative study of Delhi and Mumbai, *Environments 2*, 125-138.

Haklay, M. (2010), How good is OpenStreetMap information: A comparative study of OpenStreetMap and Ordnance Survey datasets for London and the rest of England, *Environ. Plan. B*, *37*, 682–703.

Howard, L. (1833), *The Climate of London*, Vols. I-III, W. Phillips, London.

670 Jacobson, M. Z., R. Lu, R. P. Turco, and O. B. Toon (1996), Development and application of a
671 new air pollution modeling system. Part I: Gas-phase simulations, *Atmos. Environ., 30B*,
672 1939–1963.
673 Jacobson, M. Z. (1997), Development and application of a new air pollution modeling system.
674 Part III: Aerosol-phase simulations, *Atmos. Environ., 31A*, 587–608.
675 Jacobson M. Z. (2001a), GATOR-GCMM: A global through urban scale air pollution and
676 weather forecast model. 1. Model design and treatment of subgrid soil, vegetation, roads,
677 rooftops, water, sea ice, and snow, *J. Geophys. Res*., *106*, 5385-5402.
678 Jacobson, M. Z. (2001b), GATOR-GCMM: 2. A study of day- and nighttime ozone layers aloft,
679 ozone in national parks, and weather during the SARMAP Field Campaign, *J. Geophys. Res.,*
680 *106*, 5403-5420.
681 Jacobson, M. Z. (2002), Analysis of aerosol interactions with numerical techniques for solving
682 coagulation, nucleation, condensation, dissolution, and reversible chemistry among multiple
683 size distributions, *J. Geophys. Res*., *107* (D19), 4366, doi:10.1029/ 2001JD002044.
684 Jacobson, M. Z. (2003), Development of mixed-phase clouds from multiple aerosol size
685 distributions and the effect of the clouds on aerosol removal, *J. Geophys. Res., 108* (D8),
686 4245, doi:10.1029/2002JD002691.
687 Jacobson, M. Z. (2005), Studying ocean acidification with conservative, stable numerical
688 schemes for nonequilibrium air-ocean exchange and ocean equilibrium chemistry, *J. Geophys.*
689 *Res., 110*, D07302, doi:10.1029/2004JD005220.
690 Jacobson, M. Z. (2008), The causal link between carbon dioxide and air pollution mortality,
691 *Geophysical Res. Lett., 35*, L03809, doi:10.1029/2007GL031101.

692 Jacobson, M. Z. (2012), Investigating cloud absorption effects: Global absorption properties of
693 black carbon, tar balls, and soil dust in clouds and aerosols, *J. Geophys. Res*., *117*, D06205,
694 doi:10.1029/2011JD017218.
695 Jacobson, M.Z. (2014), Effects of biomass burning on climate, accounting for heat and moisture
696 fluxes, black and brown carbon, and cloud absorption effects, *J. Geophys. Res*., *119*, 8980-
697 9002, doi:10.1002/2014JD021861.
698 Jacobson, M. Z., Y. J. Kaufmann, and Y. Rudich (2007), Examining feedbacks of aerosols to
699 urban climate with a model that treats 3-D clouds with aerosol inclusions, *J. Geophys. Res.*,
700 *112*, D24205, doi:10.1029/2007JD008922.
701 Jacobson, M. Z., and D. G. Streets (2009), The influence of future anthropogenic emissions on
702 climate, natural emissions, and air quality, *J. Geophys. Res.*, 114, D08118,
703 doi:10.1029/2008JD011476.
704 Jacobson, M. Z., and J. E. Ten Hoeve (2012), Effects of urban surfaces and white roofs on global
705 and regional climate, *J. Climate, 25*, 1028-1044, doi:10.1175/JCLI-D-11-00032.1.
706 Jacobson, M.Z., S.V. Nghiem, A. Sorichetta, and N. Whitney, (2015), *Ring of impact* from the
707 mega-urbanization of Beijing between 2000 and 2009, *J. Geophys. Res*., *120*, 5740-5756,
708 doi:10.1002/2014JD023008.
709 Ketefian, G. S., and M. Z. Jacobson (2009), A mass, energy, vorticity, and potential enstrophy
710 conserving boundary treatment scheme for the shallow water equations, *J. Comp. Phys*., *228*,
711 1-32, doi:10.1016/j.jcp.2008.08.009.
712 Koukoletsos, T., Haklay, M., and C. Ellul (2012), Assessing data completeness of VGI through
713 an automated matching procedure for linear data, *Trans. GIS, 16*, 477–498.
714 LaDochy, S., and M. Witiw (2012), The continued reduction in dense fog in the Southern
715 California region: Possible causes, *Pure and Applied Geophysics*, *169*, 1157-1163.

716 Lal, D.M., and S.D. Pawar (2011), Effect of urbanization on lightning over four metropolitan
717 cities of India, *Atmos. Environ., 45*, 191-196.
718 Li, C.C., Wang, J., Wang, L., Hu, L.Y., & Gong, P. (2014), Comparison of Classification
719 Algorithms and Training Sample Sizes in Urban Land Classification with Landsat Thematic
720 Mapper Imagery, *Remote Sensing*, *6*, 964–983.
721 Lu, R., and R. P. Turco (1995), Air pollutant transport in a coastal environment, II, Three-
722 dimensional simulations over Los Angeles basin, *Atmos. Environ.*, *29*, 1499-1518.
723 Mellor, G. L., and T. Yamada (1982), Development of a turbulence closure model for
724 geophysical fluid problems, *Rev. Geophys. Space Phys., 20*, 851-873.
725 Mohan, M., Y. Kikegawa, B.R.Gurjar, S. Bhati, and N.R. Kolli (2013). Assessment of urban heat
726 island effect for different land use-land cover from micrometeorological measurements and
727 remote sensing data for megacity Delhi, *Theoretical and Applied Climatology, 112*, 647-658.
728 Molinari, M.E., M. Minghini, G. Prestifilippo, M.A. Brovelli, and P. Mooney (2016), An open
729 source procedure to assess the quality of the OpenStreetMap road network. In Mapping,
730 Sensing, and Crowdsourcing Geographic Information (pp. 1-1).
731 MODIS/USGS Terra plus Aqua Combined Albedo 16-Day L3 Global 0.05˚ CMG V4 data,
732 https://lpdaac.usgs.gov/about/news_archive/modisterra_land_cover_types_yearly_l3_global_0
733 05deg_cmg_mod12c1 (accessed April 1, 2018).
734 Neis, P., D. Zielstra, and A. Zipf (2012), The street network evolution of crowd-sourced maps:
735 OpenStreetMap in Germany 2007–2011, *Future Internet*, *4*, 1–21.
736 Nghiem, S. V., D. Balk, E. Rodriguez, G. Neumann, A. Sorichetta, C. Small, and C. D. Elvidge
737 (2009), Observations of urban and suburban environments with global satellite scatterometer
738 data, *ISPRS J. Photogrammetry and Remote Sensing*, *64*, 367-380,
739 doi:10.1016/j.isprsjprs.2009.01.004.

740 Nghiem, S. V., A. Sorichetta, C. D. Elvidge, C. Small, D. Balk, U. Deichmann, and G. Neumann
741 (2014), Remote Sensing of Urban Environments – The Beijing Case Study, in *Encyclopedia of*
742 *Remote Sensing*, edited by E. Njoku, pp. 869-878, Springer, New York, Heidelberg, Dordrecht,
743 London.
744 Nghiem, S. V., C. Small, M. Z. Jacobson, G. R. Brakenridge, D. Balk, A. Sorichetta, M. Masetti,
745 A. E. Gaughan, F. R. Stevens, A. Mathews, A. E. Frazier, and N. N. Das (2017), Multi-
746 Sourced Satellite Observations of Land Cover and Land Use Change in South and Southeast
747 Asia with Challenging Environmental and Socioeconomic Impacts, Abstract GC51D-0834
748 presented at the 2017 Fall Meeting, AGU, San Francisco, Calif., 11-15 Dec.
749 Nguyen, L.H., S.V. Nghiem, and G.M. Henebry (2018), Expansion of major urban areas in the
750 US Great Plains from 2000 to 2009 using satellite scatterometer data, *Remote Sensing of*
751 *Environment, 204*, 524-533, doi:10.1016/j.rse.2017.10.004.
752 Niyogi, D., T. Holt, S. Zhong, P. C. Pyle, and J. Basara (2006), Urban and land surface effects on
753 the 30 July 2003 mesoscale convective system event observed in the southern Great Plains, *J.*
754 *Geophys. Res., 111*, D19107, doi:10.1029/2005JD006746.
755 Null, J. (2018), El Niño and La Niña years and intensities, http://ggweather.com/enso/oni.htm
756 (accessed September 21, 2018).
757 Oke, T. R. (1982), The energetic basis of the urban heat island, *Q. J. Royal Met. Soc., 108*, 1-24.
758 OpenStreetMap (2018), http://www.openstreetmap.org (accessed April 1, 2018).
759 Pomerantz, M., B. Pon, H. Akbari, and S.-C. Chang (2000) The effect of pavements's
760 temperatures on air temperatures in large cities, LBNL-43442,
761 https://buildings.lbl.gov/sites/default/files/2000_pomerantz_et_al_effect_of_pavement_temp
762 _on_air_temp_in_large_cities.pdf (accessed April 1, 2018).

763 QuikSCAT Mission (2014), Jet Propulsion Laboratory, California Institute of Technology,
764 https://winds.jpl.nasa.gov/missions/quikscat/ (accessed April 1, 2018).
765 Rahman, A., S. Kumar, S. Fazal, and M.A. Siddiqui (2012), Assessment of land use/landcover
766 change in the northwest district of Delhi using remote sensing and GIS techniques. *J. Indian*
767 *Soc. Remote Sensing*, *40*, 689-697.
768 Schaaf, C. et al. (2002) First Operational BRDF, albedo nadir reflectance products from MODIS,
769 *Remote. Sens. Environ.*, *83*, 135-148.
770 Sharma, R., and P.K. Joshi (2013), Monitoring urban landscape dynamics over Delhi (India)
771 using remote sensing (1998-2011) inputs. *J. Indian Soc. Remote. Sens.*, *41*, 641-650.
772 Siebritz, L.A. (2014), Assessing the accuracy of openstreetmap data in South Africa for the
773 purpose of integrating it with authoritative data (PhD dissertation, University of Cape Town).
774 Toon, O. B., C. P. McKay, T. P. Ackerman, and K. Santhanam (1989), Rapid calculation of
775 radiative heating rates and photodissociation rates in inhomogeneous multiple scattering
776 atmospheres, *J. Geophys. Res*., *94*, 16,287-16,301.
777 U.S. Census Bureau (2018a), Population, https://www.census.gov/topics/population.html
778 (accessed April 1, 2018).
779 U.S. Census Bureau (2018b), TIGER/Line® Shapefiles and TIGER/Line® Files,
780 https://www.census.gov/geo/maps-data/data/tiger-line.html (accessed April 1, 2018).
781 USEPA (United States Environmental Protection Agency) (2010), 2007/2008 Version 5 Air
782 Emissions Modeling Platforms, https://www.epa.gov/air-emissions-modeling/20072008-
783 version-5-air-emissions-modeling-platforms (Accessed August 14, 2018).
784 USGS (United States Geological Survey) (2006). Land cover type yearly L3 global 500 m V5
785 data, processed to $0.01^{o}$. [Available online at https://lpdaac.usgs.gov/].

786 USGS (United States Geological Survey) (2018), SRTM Water Body Dataset,
787 https://lta.cr.usgs.gov/srtm_water_body_dataset (accessed April 1, 2018).
788 Vahmani, P., and G.A. Ban-Weiss (2016), Impact of remotely sensed albedo and vegetation
789 fraction on simulation of urban climate in WRF –urban canopy model: A case study of the
790 urban heat island in Los Angeles, *J. Geophys. Res.*, *121*, 1511-1531.
791 Walcek, C. J. (2000), Minor flux adjustment near mixing ratio extremes for simplified yet highly
792 accurate monotonic calculation of tracer advection, *J. Geophys. Res.*, 105 (D7), 9335-9348.
793 Wang, M., Li, Q., Hu, Q., and M. Zhou (2013), Quality analysis of Open Street Map data, paper
794 presented at the *8th International Symposium on Spatial Data Quality*, Hong Kong, China.
795 Weng, Q., Hu, X., & Liu, H. (2009), Estimating impervious surfaces using linear spectral
796 mixture analysis with multitemporal ASTER images, *International Journal of Remote*
797 *Sensing*, *30*, 4807-4830.
798 Will, J. (2014), Development of an automated matching algorithm to assess the quality of the
799 OpenStreetMap road network – A case study in Göteborg, Sweden, M.S. thesis, Department
800 of Physical Geography and Ecosystem Science, Lund University.
801 World Bank (2018) India, https://data.worldbank.org/country/india (accessed April 1, 2018).
802 Yagoub, M.M. (2017), Assessment of OpenStreetMap (OSM) Data: The Case of Abu Dhabi
803 City, United Arab Emirates, *Journal of Map and Geography Libraries*, *13*, 300-319.
804 Zandbergen, P.A., D.A. Ignizio, and K.E. Lenzer (2011), Positional accuracy of TIGER 2000
805 and 2009 road networks, *Transactions in GIS*, *15*, 495-519.
806 Zhang, H., and J. Malczewski (2018), Accuracy Evaluation of the Canadian OpenStreetMap
807 Road Networks, https://ir.lib.uwo.ca/geographypub/347/, Accessed July 7, 2018.

Zhao, P., T. Jia, K. Qin, J. Shan, and C. Jiao (2015), Statistical analysis on the evolution of OpenStreetMap road networks in Beijing, *Physica A: Statistical Mechanics and its Applications*, *420*, 59-72.

Zheng, S. D., and J. H. Zheng (2014), Assessing the Completeness and Positional Accuracy of OpenStreetMap in China, in *Thematic Cartography for the Society*, *Lecture, Notes in Geoinformation and Cartography*, edited by T. Bandrova et al., , Springer International Publishing, Switzerland, doi:10.1007/978-3-319-08180-9_14.

Zielstra, D., and A. Zipf (2010), A Comparative Study of Proprietary Geodata and Volunteered Geographic Information for Germany, paper presented at the *13th AGILE international conference on geographic information science*, Guimarães, Portugal.

Zielstra, D., and H.H. Hochmair (2011), A comparative study of pedestrian accessibility to transit stations using free and proprietary network data, *Transp. Res. Rec. J. Transp. Res. Board*, *2217*, 145–152.

Zielstra, D., Hochmair, H.H., and P. Neis (2013), Assessing the effect of data imports on the completeness of OpenStreetMap – A United States case study, *Trans. GIS*, *17*, 315–334.

# Figure Captions

**Figure 1.** (a) New Delhi model domain location within India, (b) 2016 road network in the New Delhi domain from *OpenStreetMap* [2018], (c) Los Angeles model domain location within California, (d) 2010 TIGER road network in the Los Angeles domain [*U.S. Census Bureau*, 2018b].

**Figure 2.** (a) New Delhi urban fraction as determined here from the DSM method, for the year 2000; (b) Same as (a), but for 2009; (c) Estimated fraction of each grid cell that is road for New Delhi in 2000; (d) Same as (c), but for 2009. Urban fractions and road fractions range from 0-1.

**Figure 3.** Same as Figure 2, but for Los Angeles.

**Figure 4.** Comparison of modeled January and July 2013 air temperatures over the India and California domains (Table 3) with *GFS* [2018] reanalysis data. The model results were from the January and July 2013 nested simulations performed here using the 2009 urban fractions. The GFS monthly average fields (at 0.5 degree resolution) were obtained by averaging data from 32 days (January 1, 12 GMT to February 1, 12 GMT and July 1, 12 GMT to August 1, 12 GMT, 2013) and 4 times per day (00 GMT, 06 GMT, 12 GMT, and 18 GMT). Numbers in parentheses are domain-averaged values. Figure S3 shows additional comparisons.

**Figure 5.** New Delhi modeled differences (2009 minus 2000) in (a) surface roughness length for momentum, (b) 15-m shearing stress, (c) the vertical component of near-surface turbulent kinetic energy (TKE), (d) 15-m wind speed, (e) soil moisture, (f) 15-m water vapor, (g) 15-m air

849 temperature, (h) 15-m relative humidity, (i) ground temperature, (j) surface latent heat flux, (k)
850 surface sensible heat flux, (l) surface albedo, (m) surface net down minus up solar plus thermal-
851 infrared (TIR) radiation, and (n) 15-m ozone for January (left panel in each pair) and July (right
852 panel in each pair) from the innermost model domain due solely to the urban extent and road
853 network changes in Figure 2 and the corresponding changes in surface properties (see text).
854
855 **Figure 6.** Los Angeles modeled differences (2009 minus 2000) in several parameters for January
856 (left panel in each pair) and July (right panel in each pair) from the innermost model domain due
857 solely to the urban extent and road network changes in Figure 3 and the corresponding changes
858 in surface properties (see text).
859
860 **Figure 7.** Vertical profiles of New Delhi domain averaged modeled differences (January 2009
861 minus January 2000) in several parameters.
862
863 **Figure 8.** Vertical profiles of New Delhi domain averaged modeled differences (July 2009 minus
864 July 2000) in several parameters.
865
866 **Figure 9.** Vertical profiles of Los Angeles domain averaged modeled differences (January 2009
867 minus January 2000) in several parameters.
868
869 **Figure 10.** Vertical profiles of Los Angeles domain averaged modeled differences (July 2009
870 minus July 2000) in several parameters.
871
872

873 **Table 1.** Total road length (valid for 2016) for each OSM road type over New Delhi calculated using the method
874 described in the text. Total area is just length multiplied by width. Wind and standard error are taken from Jacobson
875 et al. [2015].

| Class | Road type | Total length (km) 2016 | Mean Width (m) | Standard Error (m) | Total area ($km^2$) 2016 |
|---|---|---|---|---|---|
| 1 | Unclassified | 19259.7 | 7.98 | 1.14 | 153.69 |
| 2 | Trunk link | 85.2 | 6.35 | 0.80 | 0.54 |
| 3 | Trunk | 5021.8 | 23.09 | 2.70 | 115.95 |
| 4 | Track | 3583.7 | 4.21 | 0.81 | 15.09 |
| 5 | Tertiary link | 83.5 | 20.54 | 4.49 | 1.72 |
| 6 | Tertiary | 18281.4 | 17.92 | 1.46 | 327.60 |
| 7 | Steps | 4.7 | 4.07 | 0.78 | 0.02 |
| 8 | Service | 3960.1 | 9.95 | 1.80 | 39.40 |
| 9 | Secondary link | 34.1 | 9.55 | 0.65 | 0.33 |
| 10 | Secondary | 5934.6 | 27.42 | 4.19 | 162.73 |
| 11 | Residential | 15136.6 | 12.18 | 1.72 | 184.36 |
| 12 | Raceway | 7.1 | 21.20 | 0.24 | 0.15 |
| 13 | Primary link | 55.1 | 13.93 | 1.17 | 0.77 |
| 14 | Primary | 4171.7 | 24.49 | 5.05 | 102.16 |
| 15 | Pedestrian | 28.1 | 9.09 | 1.95 | 0.26 |
| 16 | Path | 115.8 | 2.14 | 0.23 | 0.25 |
| 17 | Motorway link | 46.6 | 10.33 | 0.87 | 0.48 |
| 18 | Motorway | 369.2 | 28.70 | 2.61 | 10.60 |
| 19 | Living street | 699.8 | 7.18 | 1.37 | 5.02 |
| 20 | Footway | 158.9 | 2.32 | 0.35 | 0.37 |
| 21 | Cycleway | 17.2 | 5.12 | 0.94 | 0.09 |
| 22 | Construction | 458.2 | 10.23 | 1.30 | 4.69 |
| 23 | Bridleway | 3.8 | 15.28 | 0.62 | 0.06 |
| | **Total or mean** | **77,517** | **14.53** | **1.90** | **1126.3** |

876

877 **Table 2.** Total road length (valid for 2010) for each TIGER road type over Los Angeles calculated using the method
878 described in the text. Total area is just length multiplied by width. Wind and standard error are taken from Jacobson
879 et al. [2015].

| Class | Road type | Total length (km) 2010 | Mean Width (m) | Standard Error (m) | Total area ($km^2$) 2010 |
|---|---|---|---|---|---|
| 1 | Primary road | 7247.9 | 24.49 | 5.05 | 177.50 |
| 2 | Secondary road | 12153.0 | 27.42 | 4.19 | 333.24 |
| 3 | Residential | 158986.1 | 12.18 | 1.72 | 1936.45 |
| 4 | Vehicular trail | 3318.3 | 10.0 | 1.9 | 33.18 |
| 5 | Ramp | 2464.3 | 6.35 | 0.80 | 15.65 |
| 6 | Service drive | 377.3 | 9.95 | 1.80 | 3.75 |
| 7 | Walkway/trail | 197.1 | 9.09 | 1.95 | 1.79 |
| 8 | Stairway | 0.1 | 4.07 | 0.78 | 0.00036 |
| 9 | Alley | 1159.0 | 6.1 | 0.75 | 7.07 |
| 10 | Private road | 4814.8 | 10.23 | 1.30 | 49.26 |
| 11 | Private driveway | 173.3 | 6.1 | 0.75 | 1.06 |
| 12 | Parking lot road | 30.2 | 9.95 | 1.80 | 0.30 |
| 13 | Bike path/trail | 3.2 | 5.0 | 0.6 | 0.02 |
| | **Total or mean** | **190,924** | **13.40** | **1.98** | **1126.3** |

880

881

882 **Table 3.** Resolutions of the nested domains treated here for each Case 1 (New Delhi) and Case 2 (Los Angeles).

| Domain | S-N Resolution | W-E Resolution | # S-N cells | # W-E cells | Center of Southernmost Cell | Center of Westernmost Cell | Number layers |
|---|---|---|---|---|---|---|---|
| Case 1 | | | | | | | |
| Global* | $4^o$ | $5^o$ | 44 | 72 | 86 S | 180 W | 68 |
| India | $0.33^o$ | $0.46^o$ | 146 | 156 | 3.485 N | 35.1 E | 55 |
| New Delhi | $0.017^o$ | $0.025^o$ | 146 | 156 | 27.3 N | 75.15 E | 55 |
| Case 2 | | | | | | | |
| Global* | $4^o$ | $5^o$ | 44 | 72 | 86 S | 180 W | 68 |
| California | $0.20^o$ | $0.15^o$ | 60 | 95 | 30 N | 129 W | 55 |
| Los Angeles | $0.0181807^o$ | $0.030414^o$ | 146 | 156 | 32.452789 N | 120.730939 W | 55 |

883 *The S-N resolution of the global domain is $6^o$ for the southernmost and northernmost grid cells, but the centers are
884 considered to be 86 S and 86 N, respectively (thus the next centers are 82 S and 82 N, respectively).
885

886

887
888

889 **Table 4.** Modeled New Delhi domain averaged 2000 values and 2009 minus 2000 values, averaged over each January and July.

| Species | 2000 Baseline January | 2009 minus 2000 January (% change) | 2000 Baseline July | 2009 minus 2000 July (% change) |
|---|---|---|---|---|
| Surface roughness (m) | 0.167 | +24.5 | 0.162 | +25.3 |
| Shear stress (kg/m/s) | 0.058 | +1.91 | 0.19 | +0.74 |
| Turbulent kinetic energy ($m^2/s^2$) | 0.13 | +1.48 | 0.52 | +0.55 |
| 15-m wind speed (m/s) | 2.75 | -0.36 | 4.79 | -0.76 |
| 38-m wind speed (m/s) | 4.03 | -0.45 | 6.01 | -0.60 |
| 100-m wind speed (m/s) | 4.97 | -0.37 | 7.64 | -0.43 |
| Soil moisture ($m^3/m^3$) (land only) | 0.19 | -1.92 | 0.25 | -0.92 |
| Surface $H_2O$(g) (ppmv) | 7,000 | -0.15 | 2,902 | +0.074 |
| Ground temp. (K) | 282.2 | -0.025 | 307.1 | -0.014 |
| 15-m air temp. (K) | 283.6 | +0.013 | 303.7 | -0.0012 |
| 38-m air temp. (K) | 284.4 | +0.01 | 303.7 | -0.0013 |
| Surface relative humidity (%) | 55.2 | -0.39 | 62.6 | +0.064 |
| Latent heat flux (LHF) ($W/m^2$) (+ is up) | 19.3 | +0.68 | 134 | +0.27 |
| Sensible heat flux (SHF) ($W/m^2$) (+ is up) | -1.69 | -19.3 | 6.44 | +4.08 |
| Surface albedo | 0.14 | -0.22 | 0.14 | -0.22 |
| Surface TIR irrad ($W/m^2$) (+ down) | -85.5 | -0.13 | -89.3 | -0.06 |
| Surface solar irrad ($W/m^2$) (+ down) | 125 | +0.044 | 220 | +0.26 |
| Surf down-up Sol+TIR ($W/m^2$) (+ down) | 39.9 | +0.42 | 131 | +0.48 |
| Surface UV irradiance ($W/m^2$) | 5.29 | -0.06 | 12.9 | +0.051 |
| LHF+SHF-Sol-TIR (+ is up) | -22.27 | -1.31 | 9.79 | -0.0019 |
| Activated CCN ($No/cm^3$) | 372 | +0.16 | 740 | -1.67 |
| Activated IDN ($No/cm^3$) | 0.0054 | +1.17 | 0.0072 | +0.46 |
| 650-nm cloud optical depth | 2.31 | +1.17 | 4.72 | -0.26 |
| Cloud absorption optical depth | 0.0010 | +1.90 | 0.0017 | +2.75 |
| Cloud liquid mass ($kg/m^2$) | 0.0078 | +0.61 | 0.053 | -0.79 |
| Cloud ice mass ($kg/m^2$) | 0.021 | +0.50 | 0.050 | -0.39 |
| Cloud fraction | 0.23 | +0.39 | 0.53 | -0.23 |
| Precipitation (mm/day) | 3.60 | -0.37 | 19.5 | -1.22 |
| Lightning flash rate ($flashes/km^2/yr$) | 554 | -0.70 | 2,510 | -1.2 |
| Surface daytime $O_3$ (ppbv) | 55.9 | +0.52 | 52.0 | +0.72 |
| Surface $O_3$ (ppbv) | 46.2 | +0.69 | 35.4 | +0.81 |
| Surface PAN (ppbv) | 2.60 | +0.033 | 0.42 | +1.54 |
| Surface CO (ppbv) | 665 | -0.45 | 299 | +0.63 |
| Column $H_2O$ ($kg/m^2$) | 9.96 | +0.12 | 62.5 | -0.093 |
| Column $O_3$ ($g/m^2$) | 6.17 | +0.027 | 5.88 | +0.054 |
| Column PAN ($g/m^2$) | 0.011 | +0.44 | 0.008 | +1.12 |
| Column CO ($g/m^2$) | 1.03 | +0.18 | 0.95 | +0.57 |
| Surface $PM_{2.5}$ ($\mu g/m^3$) | 88.3 | -0.24 | 76.8 | +0.85 |
| Surface dry $PM_{2.5}$ ($\mu g/m^3$) | 80.5 | -0.17 | 72.5 | +0.88 |
| Surface all-size BC ($\mu g/m^3$) | 4.52 | -0.34 | 0.99 | +0.53 |
| Surface all-size $H_2O$(aq) ($\mu g/m^3$) | 8.03 | -0.76 | 5.26 | +0.026 |
| Surface all-size $Na^+$ ($\mu g/m^3$) | 0.80 | -0.045 | 0.88 | +0.19 |
| Surface all-size soil dust ($\mu g/m^3$) | 26.3 | +0.74 | 96.8 | +1.47 |
| Clear-sky 550-nm AOD | 0.33 | +0.16 | 0.36 | +1.97 |
| Col. aerosol number ($No/cm^2$) | $7.3x10^9$ | +0.11 | $6.9x10^9$ | +0.43 |
| Column dry aerosol mass ($mg/m^2$) | 159 | +0.28 | 356 | +2.24 |
| Column BC ($mg/m^2$) | 2.45 | +0.25 | 0.69 | +0.31 |
| Column aer-$H_2O$(aq) ($mg/m^2$) | 6.76 | +0.97 | 16.5 | -2.66 |
| Column $Na^+$ ($mg/m^2$) | 1.26 | +0.12 | 1.27 | +0.54 |
| Column soil dust ($mg/m^2$) | 112 | +0.34 | 332 | +2.35 |

890 Divide $mg/m^2$ by 1.9637 to obtain Tg. TIR=thermal infrared. UV=ultraviolet. TKE=turbulence kinetic
891 energy. CCN=cloud condensation nuclei. IDN=ice deposition nuclei. AOD=aerosol optical depth.
892 $PM_{2.5}$=particles below 2.5 $\mu$m in diameter.
893

**Table 5.** Modeled Los Angeles domain averaged 2000 values and 2009 minus 2000 values, averaged over each January and July.

| Species | 2000 Baseline January | 2009 minus 2000 January (% change) | 2000 Baseline July | 2009 minus 2000 July (% change) |
|---|---|---|---|---|
| Surface roughness (m) | 0.205 | +18.0 | 0.200 | +18.7 |
| Shear stress (kg/m/s) | 0.16 | +1.22 | 0.067 | +2.11 |
| Turbulent kinetic energy ($m^2/s^2$) | 0.36 | +0.63 | 0.16 | +1.12 |
| 15-m wind speed (m/s) | 4.92 | -0.28 | 3.25 | -0.39 |
| 38-m wind speed (m/s) | 5.56 | -0.27 | 3.66 | -0.31 |
| 100-m wind speed (m/s) | 6.24 | -0.20 | 3.89 | -0.18 |
| Soil moisture ($m^3/m^3$) (land only) | 0.14 | -1.24 | 0.078 | +3.34 |
| Surface $H_2O$(g) (ppmv) | 6,031 | -0.025 | 16,700 | -0.035 |
| Ground temp. (K) | 279.7 | +0.003 | 301.2 | -0.015 |
| 15-m air temp. (K) | 277.9 | +0.008 | 294.8 | +0.004 |
| 38-m air temp. (K) | 278.0 | +0.006 | 295.0 | +0.003 |
| Surface relative humidity (%) | 64.3 | -0.17 | 67.1 | -0.072 |
| Latent heat flux ($W/m^2$) (+ is up) | 45.6 | +0.029 | 39.9 | +0.31 |
| Sensible heat flux ($W/m^2$) (+ is up) | 13.2 | +2.87 | 32.0 | +0.39 |
| Surface albedo | 0.124 | -0.56 | 0.11 | -0.56 |
| Surface TIR irrad ($W/m^2$) (+ down) | -99.4 | +0.028 | -130.4 | -0.16 |
| Surface solar irrad ($W/m^2$) (+ down) | 126.3 | +0.094 | 287.9 | -0.067 |
| Surf down-up Sol+TIR ($W/m^2$) (+ down) | 26.9 | +0.34 | 157.5 | +0.007 |
| Surface UV irradiance ($W/m^2$) | 5.61 | -0.002 | 14.3 | -0.48 |
| LHF+SHF-Sol-TIR (+ is up) | 31.9 | +0.95 | -85.5 | -0.28 |
| Activated CCN ($No/cm^3$) | 95.9 | +1.1 | 156 | +2.24 |
| Activated IDN ($No/cm^3$) | 0.00073 | +0.079 | 0.0010 | +1.84 |
| 650-nm cloud optical depth | 1.12 | -0.095 | 0.63 | +2.17 |
| Cloud absorption optical depth | 0.00007 | +1.25 | 0.00006 | +1.34 |
| Cloud liquid mass ($kg/m^2$) | 0.0058 | +0.25 | 0.0037 | +1.92 |
| Cloud ice mass ($kg/m^2$) | 0.0067 | +0.0025 | 0.0089 | +3.13 |
| Cloud fraction | 0.15 | +0.38 | 0.13 | +1.32 |
| Precipitation (mm/day) | 1.75 | +0.28 | 1.84 | +3.97 |
| Surface daytime $O_3$ (ppbv) | 37.9 | +0.26 | 53.5 | -0.36 |
| Surface $O_3$ (ppbv) | 36.1 | +0.36 | 45.8 | +0.25 |
| Surface PAN (ppbv) | 0.29 | +0.17 | 0.44 | -1.81 |
| Surface CO (ppbv) | 134 | -0.063 | 116 | -0.61 |
| Column $H_2O$ ($kg/m^2$) | 8.99 | -0.015 | 27.3 | -0.22 |
| Column $O_3$ ($g/m^2$) | 6.57 | +0.0015 | 6.24 | -0.039 |
| Column PAN ($g/m^2$) | 0.0037 | +0.14 | 0.0087 | -0.81 |
| Column CO ($g/m^2$) | 0.74 | +0.088 | 0.65 | -0.45 |
| Surface $PM_{2.5}$ ($\mu g/m^3$) | 34.2 | -0.80 | 27.7 | -4.69 |
| Surface dry $PM_{2.5}$ ($\mu g/m^3$) | 21.4 | -0.42 | 20.3 | -6.50 |
| Surface all-size BC ($\mu g/m^3$) | 0.53 | +0.25 | 0.68 | -1.12 |
| Surface all-size $H_2O$(aq) ($\mu g/m^3$) | 20.7 | -1.14 | 13.1 | +0.28 |
| Surface all-size $Na^+$ ($\mu g/m^3$) | 3.42 | +0.10 | 0.62 | +0.53 |
| Surface all-size soil dust ($\mu g/m^3$) | 13.5 | -0.77 | 11.2 | -0.26 |
| Clear-sky 550-nm AOD | 0.195 | -0.097 | 0.15 | -1.14 |
| Col. aerosol number ($No/cm^2$) | $5.0 \times 10^9$ | +0.11 | $7.4 \times 10^9$ | -0.40 |
| Column dry aerosol mass ($mg/m^2$) | 57.0 | -0.16 | 43.0 | -5.6 |
| Column BC ($mg/m^2$) | 0.42 | +0.43 | 0.67 | -1.19 |
| Column aer-$H_2O$(aq) ($mg/m^2$) | 25.3 | -0.40 | 4.92 | +1.01 |
| Column $Na^+$ ($mg/m^2$) | 5.94 | -0.017 | 0.42 | -0.082 |
| Column soil dust ($mg/m^2$) | 25.2 | -0.39 | 8.76 | -0.24 |

Divide $mg/m^2$ by 1.9637 to obtain Tg. TIR=thermal infrared. UV=ultraviolet. TKE=turbulence kinetic energy. CCN=cloud condensation nuclei. IDN=ice deposition nuclei. AOD=aerosol optical depth. $PM_{2.5}$=particles below 2.5 $\mu$m in diameter.

**Figure 1**

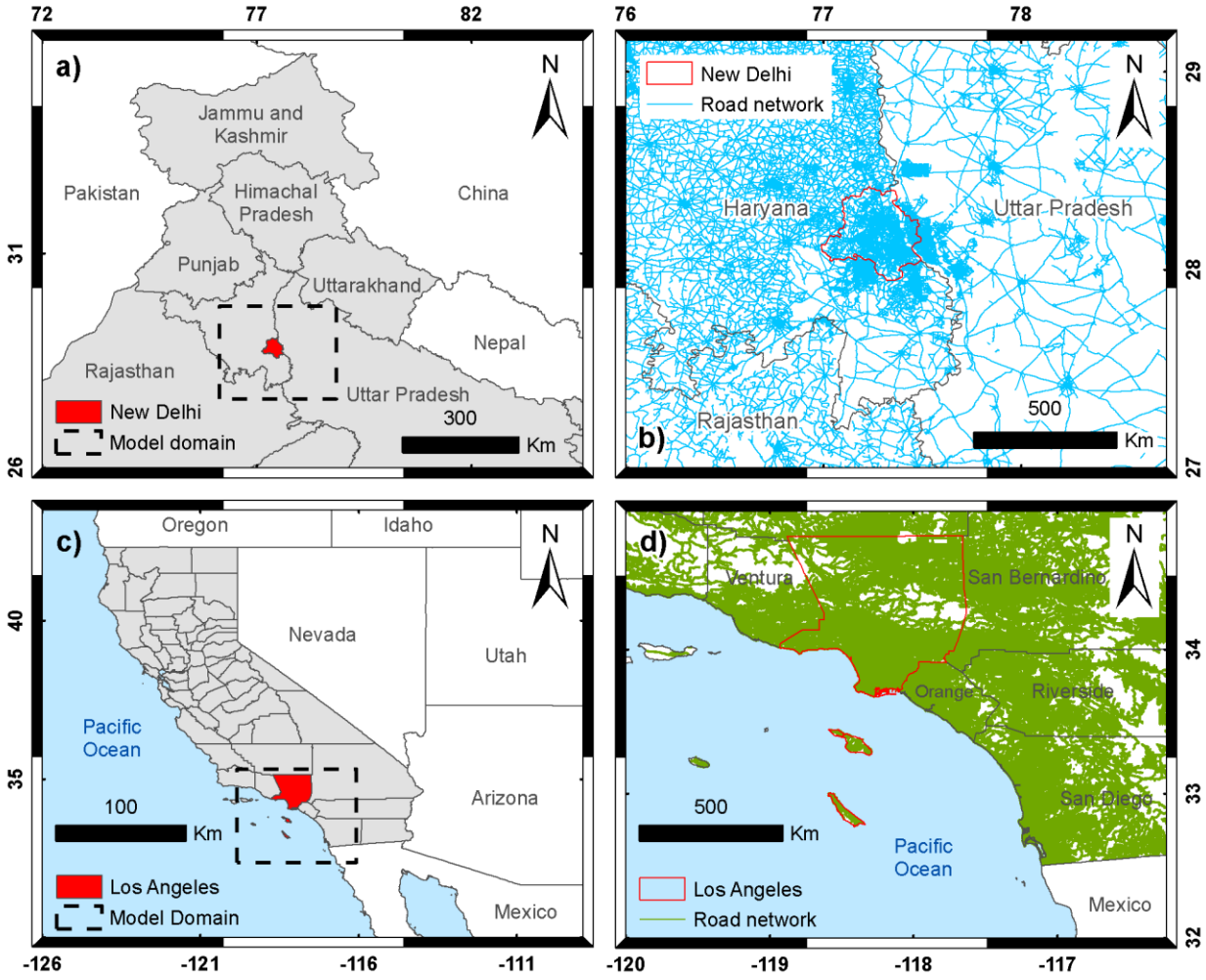


**Figure 2**

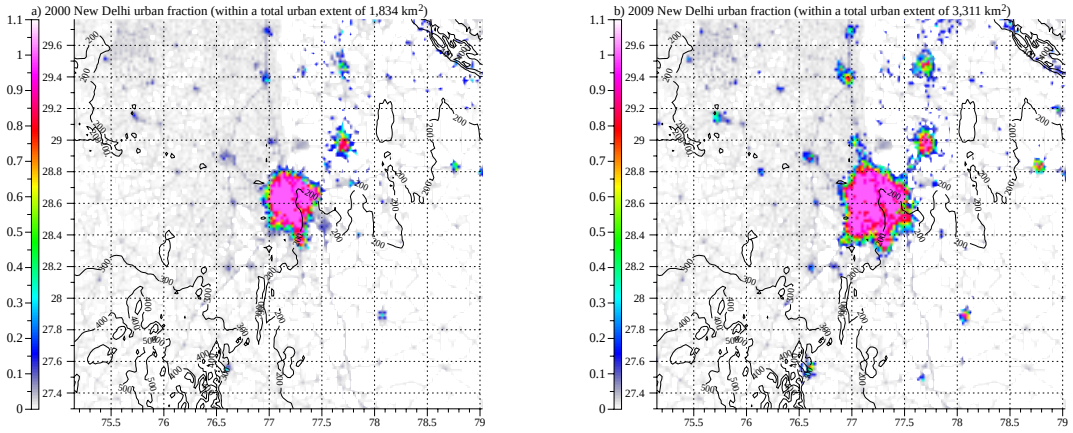

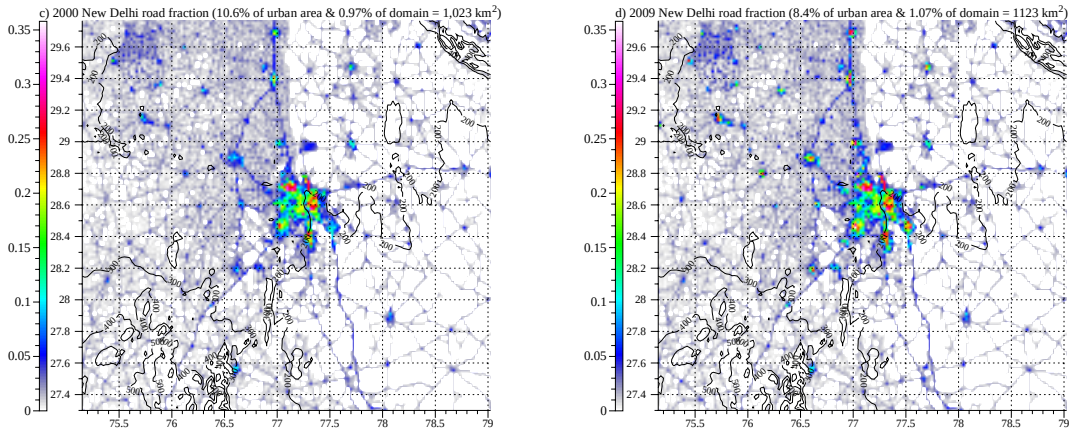


907
908

909 **Figure 3**

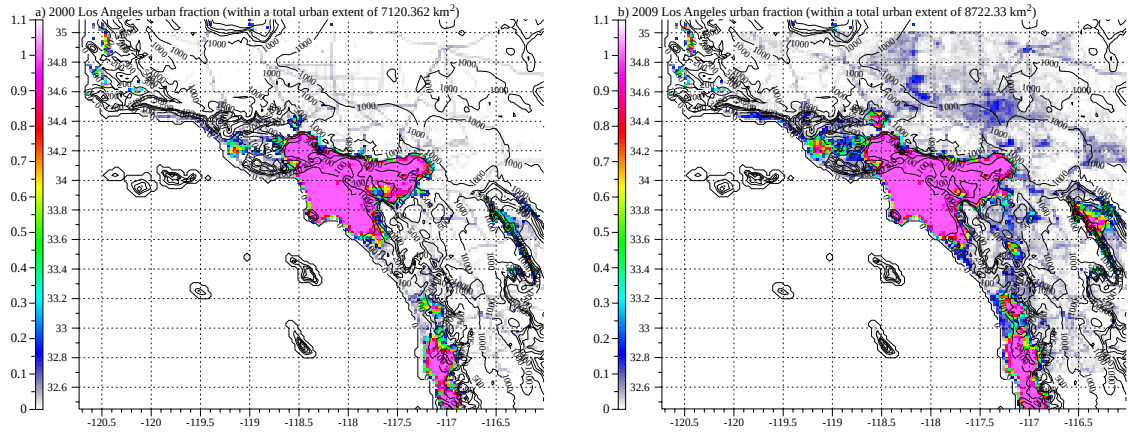


910
911

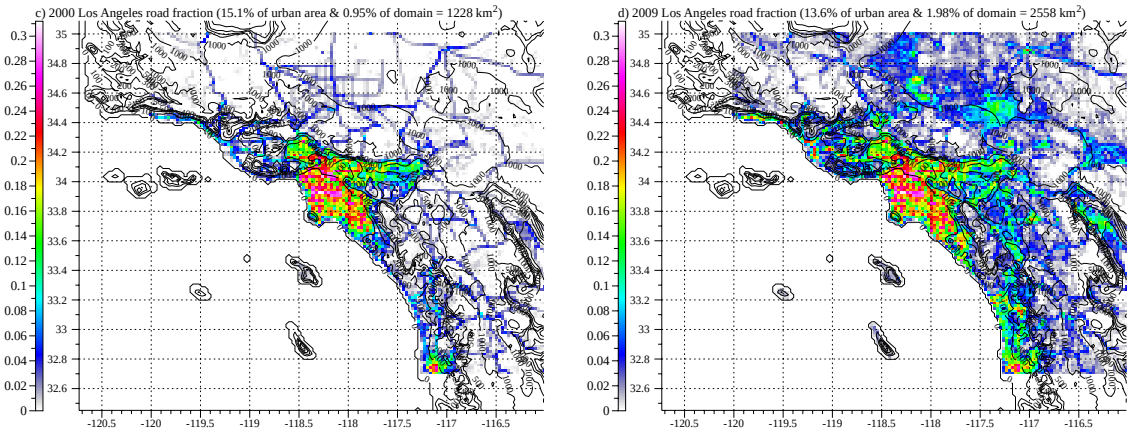


912
913
914

**Figure 4**

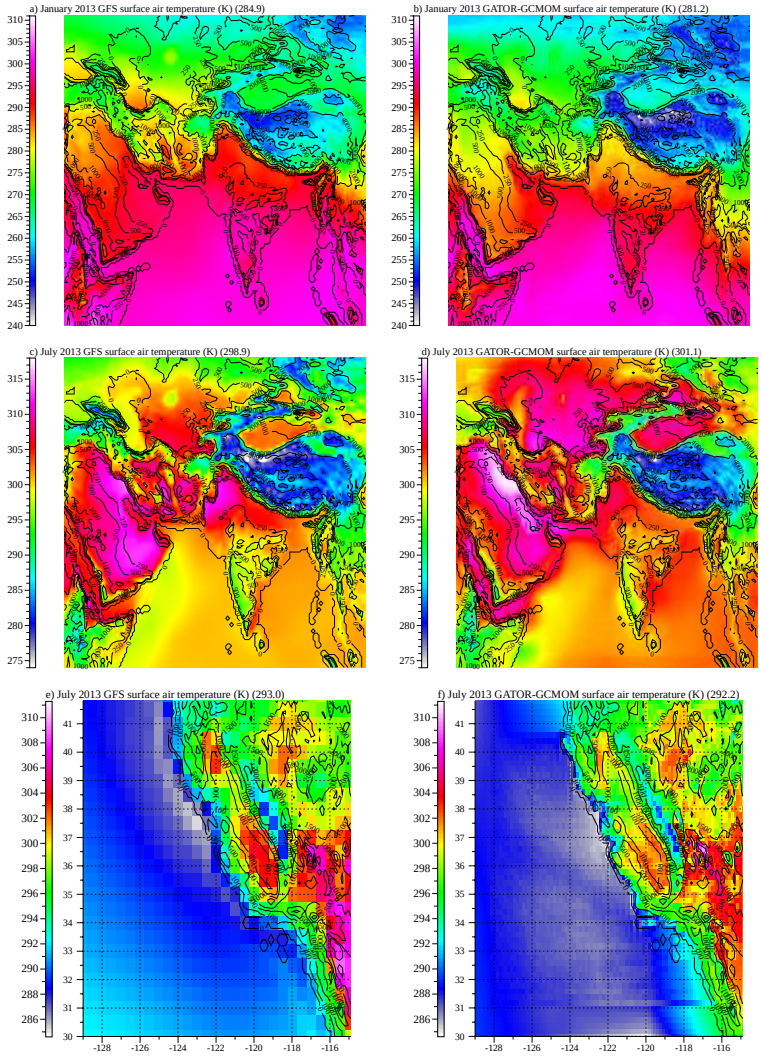
a) January 2013 GFS surface air temperature (K) (284.9)
b) January 2013 GATOR-GCMOM surface air temperature (K) (281.2)
c) July 2013 GFS surface air temperature (K) (298.9)
d) July 2013 GATOR-GCMOM surface air temperature (K) (301.1)
e) July 2013 GFS surface air temperature (K) (293.0)
f) July 2013 GATOR-GCMOM surface air temperature (K) (292.2)

**Figure 5.** New Delhi Differences (Jan, left; July, right)

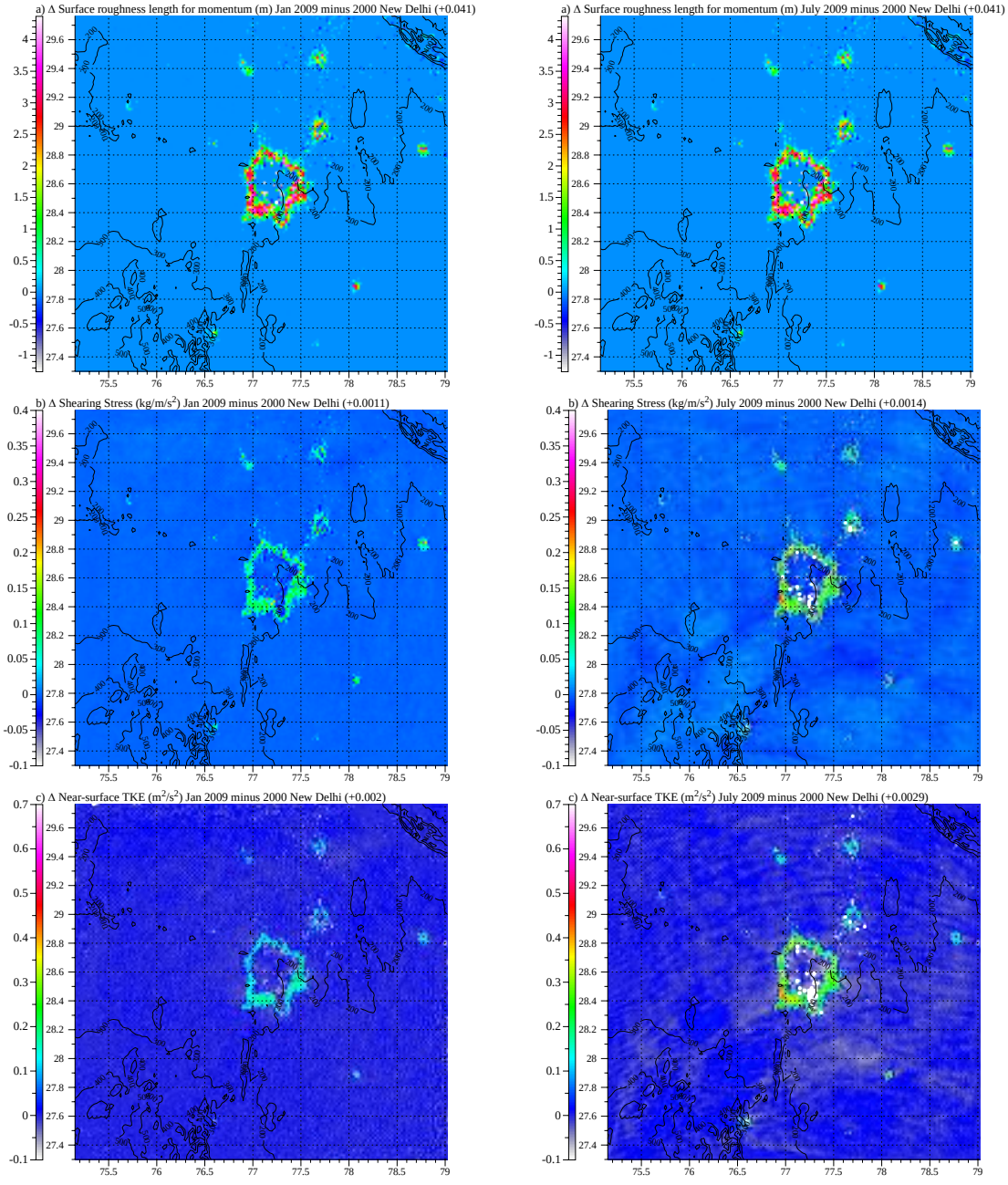

928

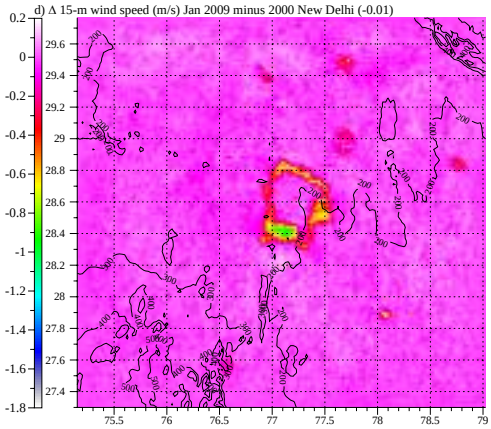


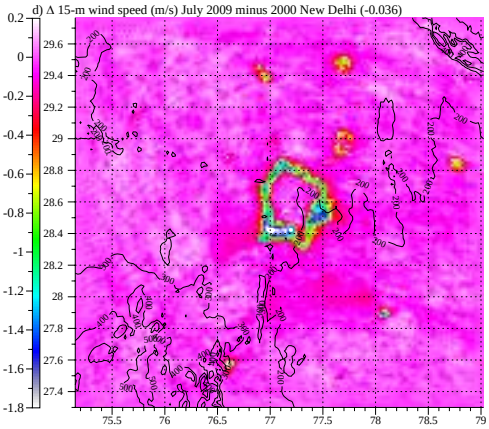


929

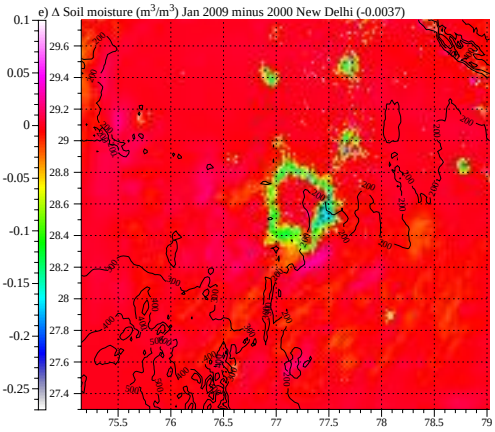


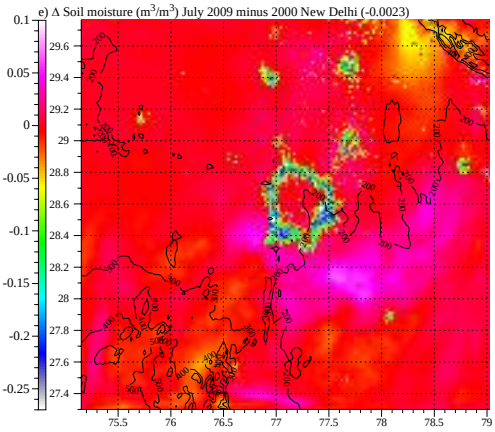


930

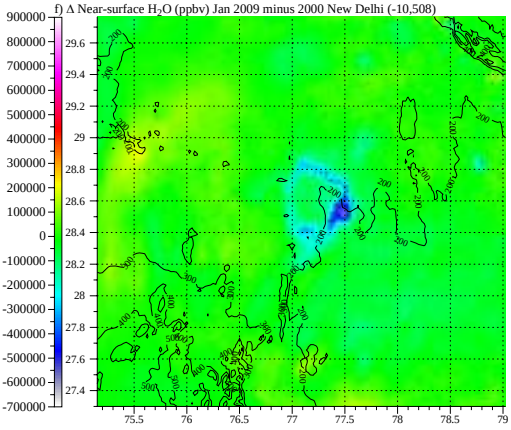


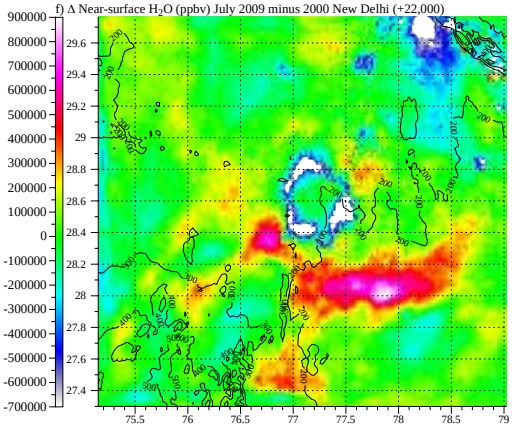


931

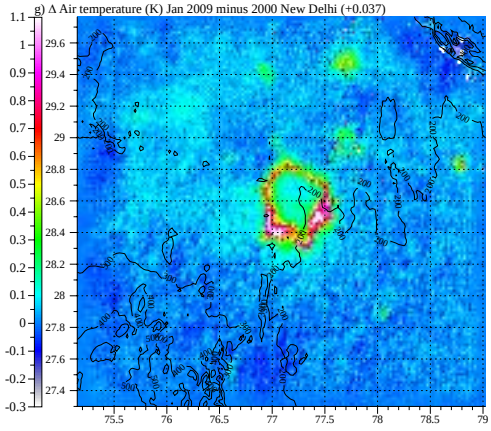


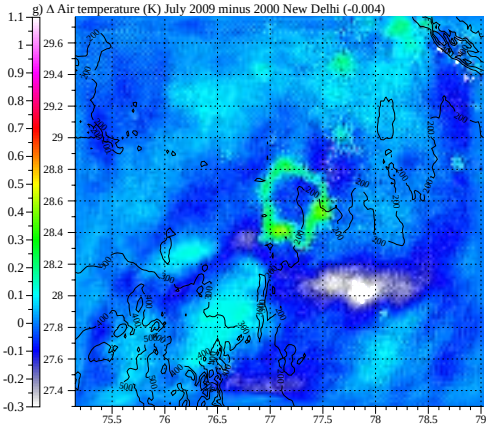

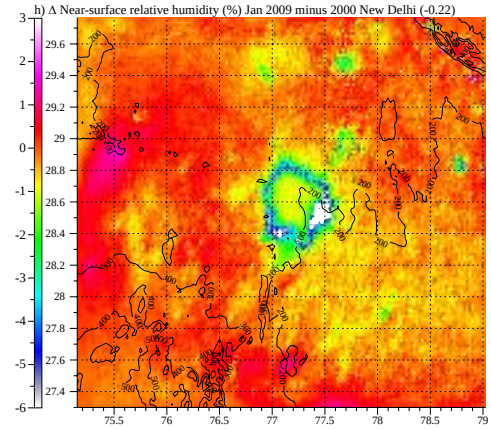


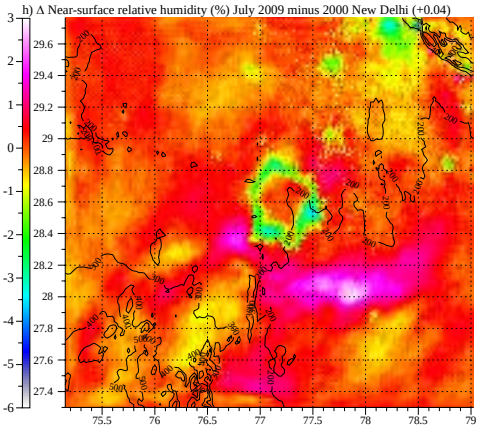


932

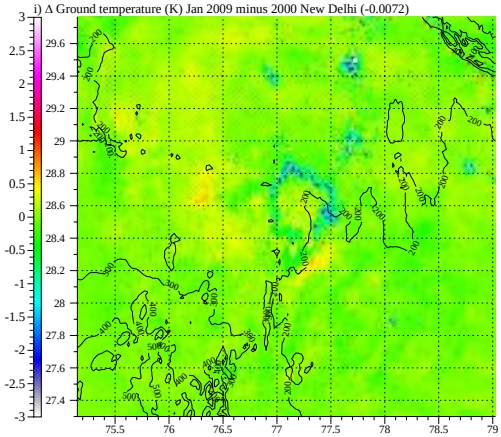


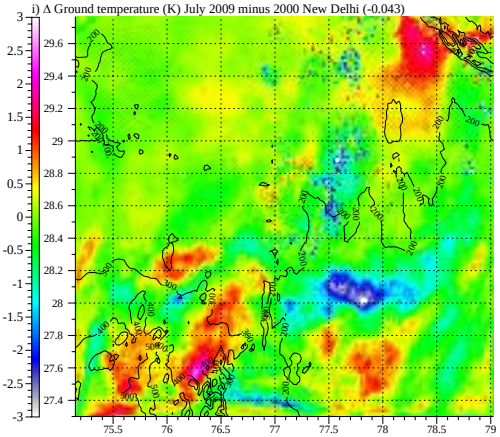


933

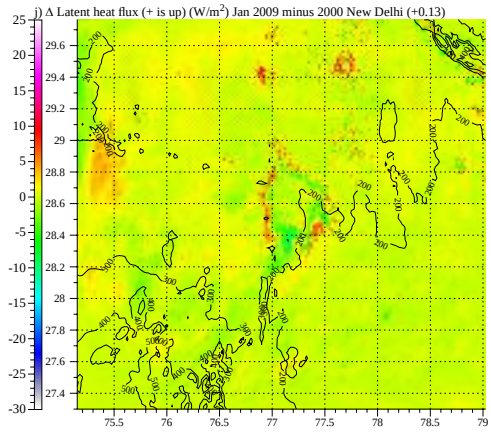


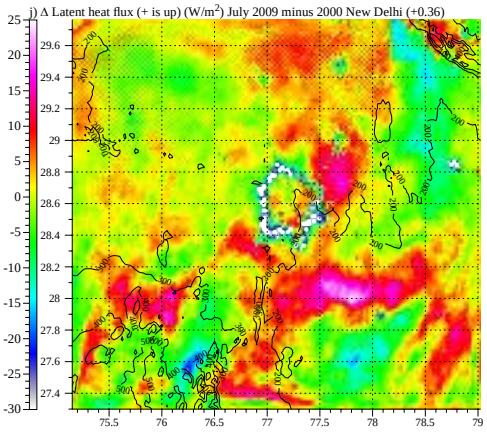


934

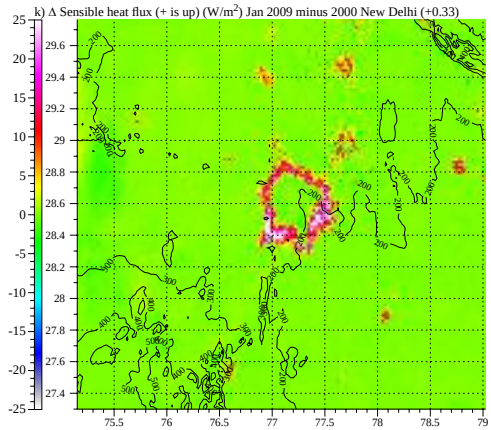


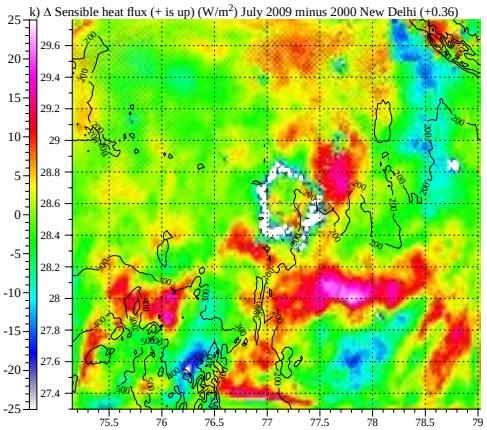


935

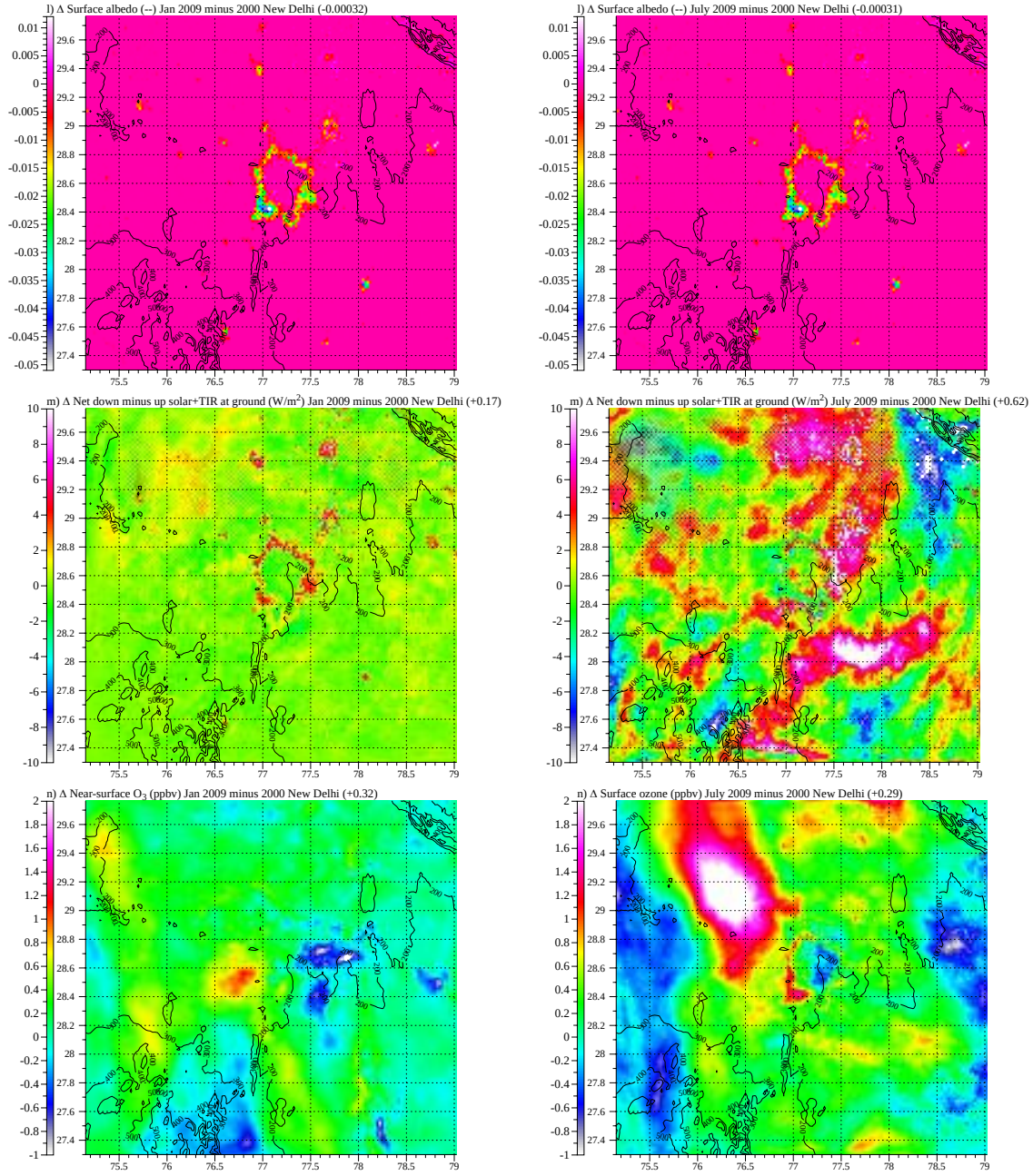


**Figure 6.** Los Angeles Differences (Jan, left; July, right)

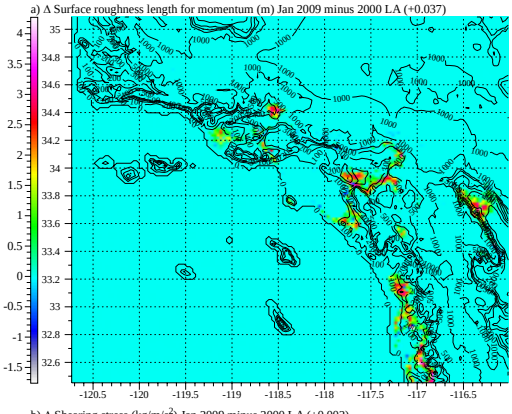


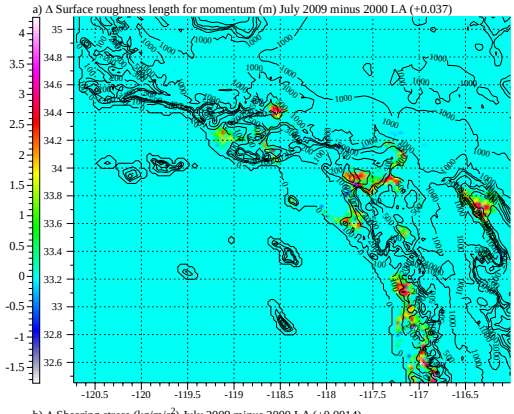


942

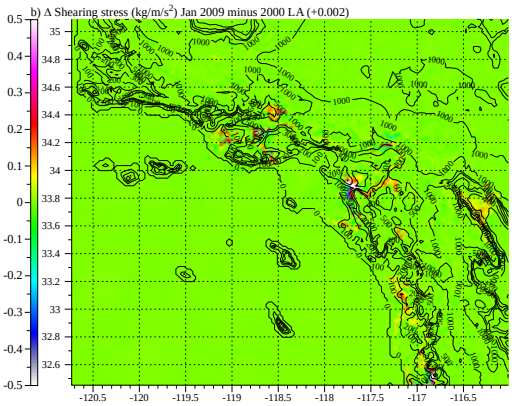


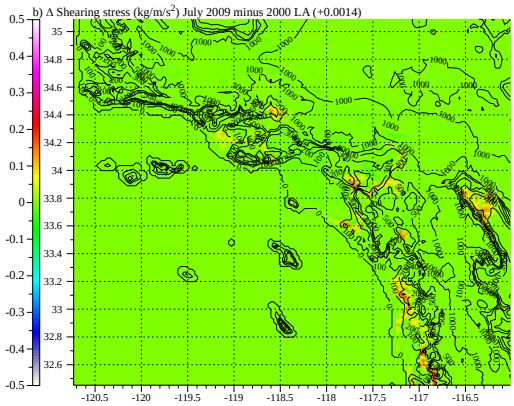


943

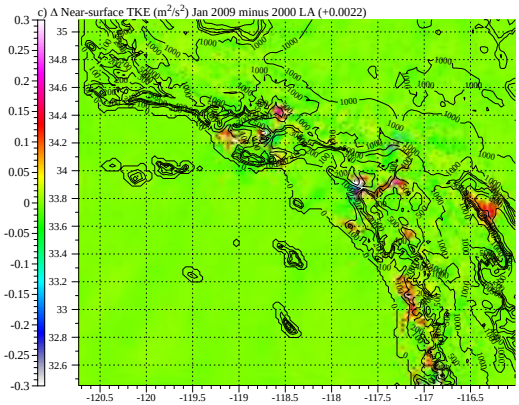


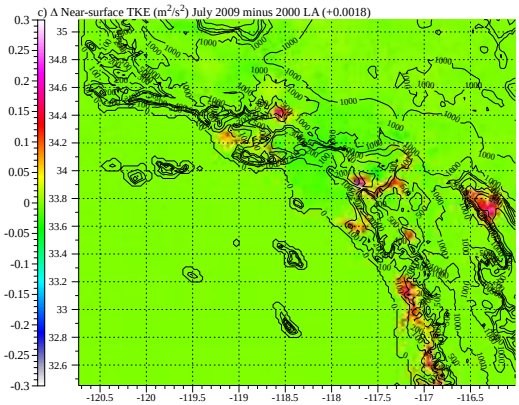


944

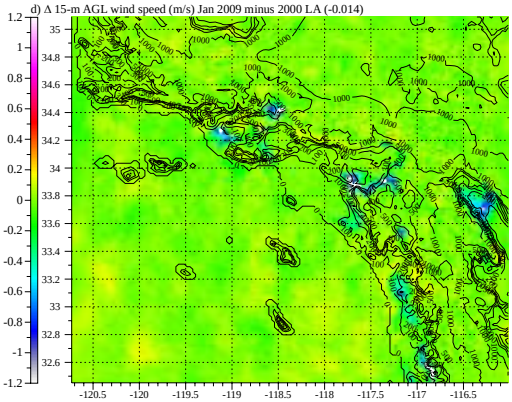


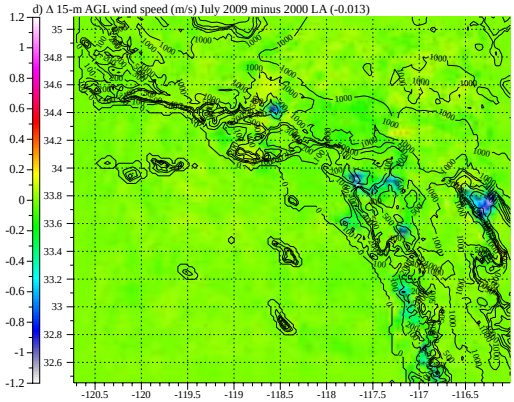


945

946

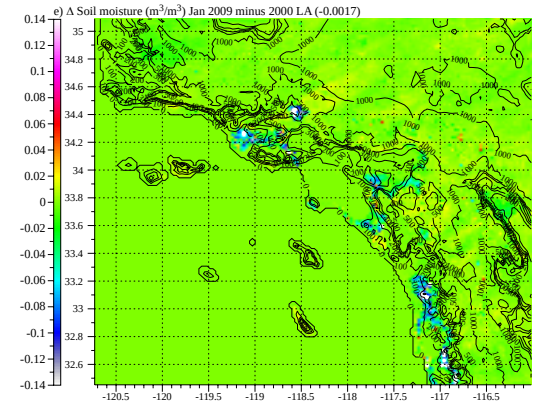


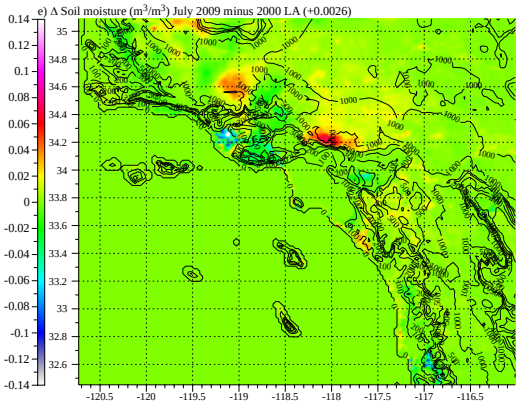


947

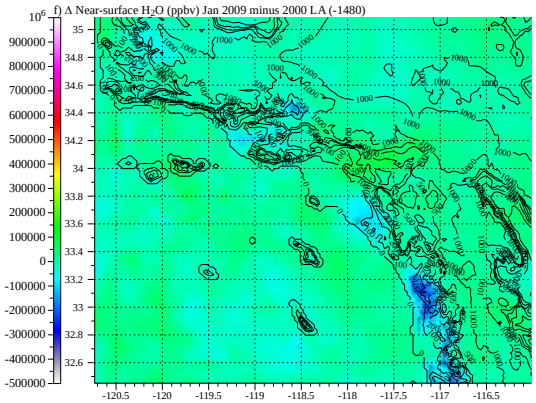


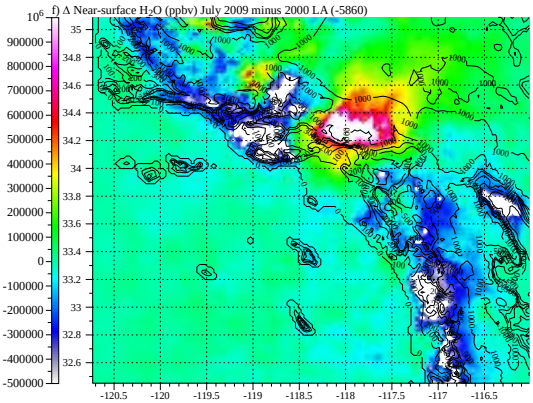


948

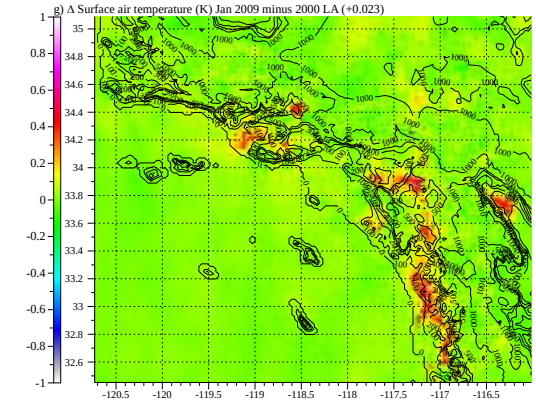


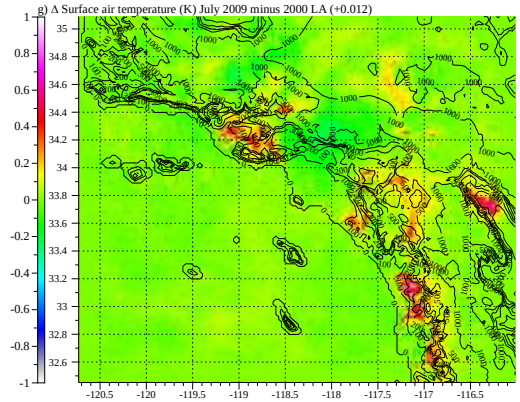


949

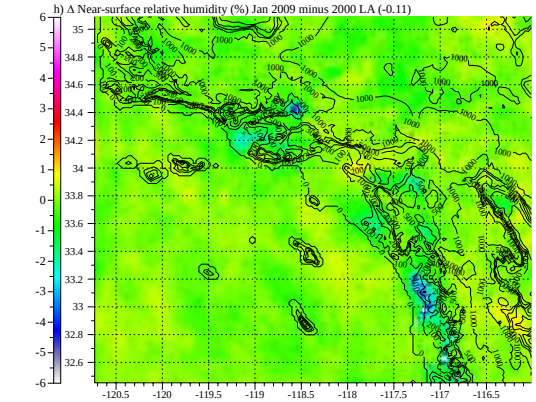


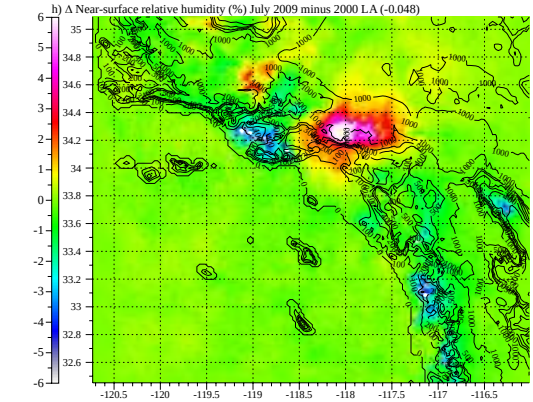

950

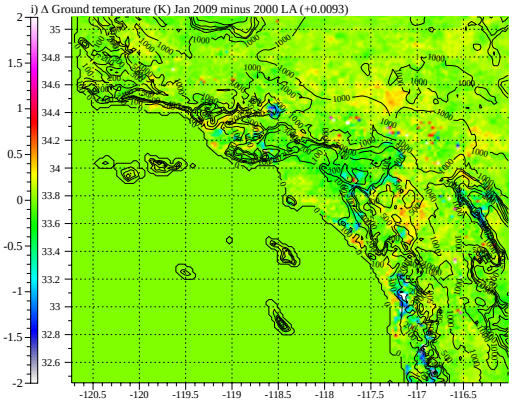


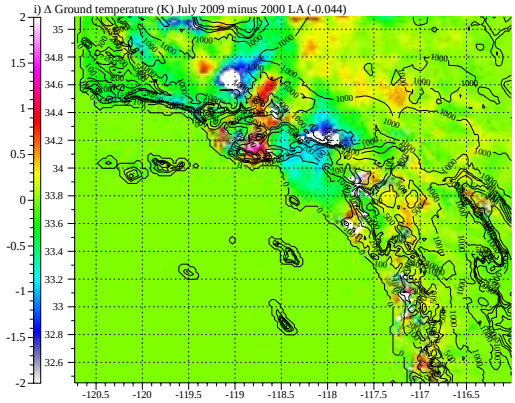


951

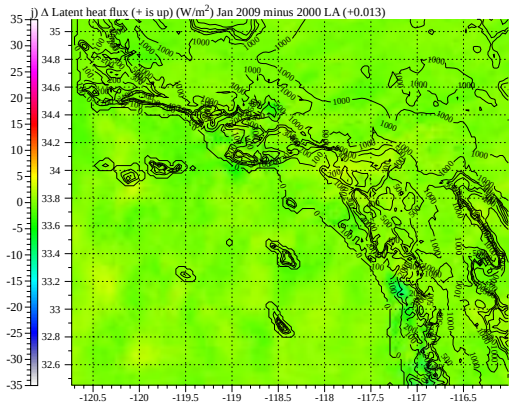


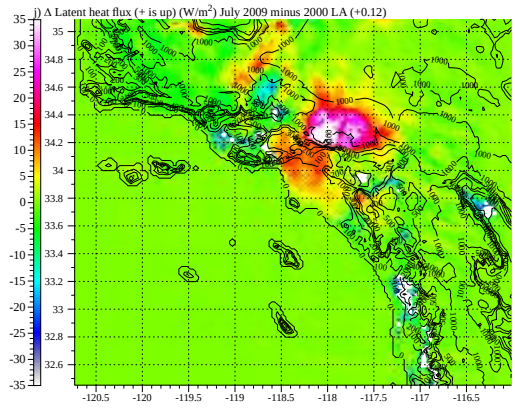


952

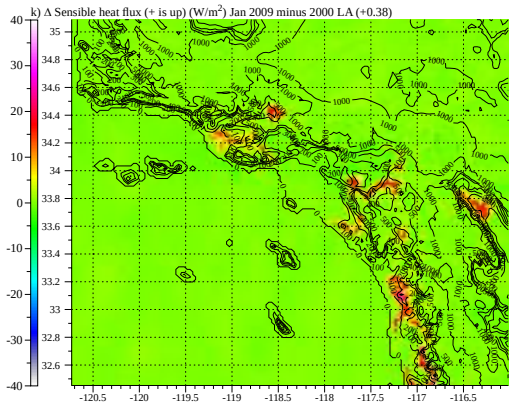


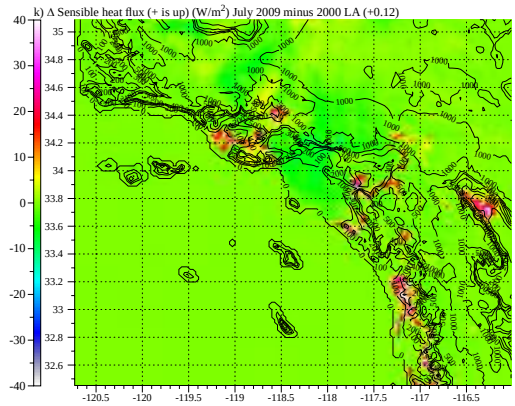


953

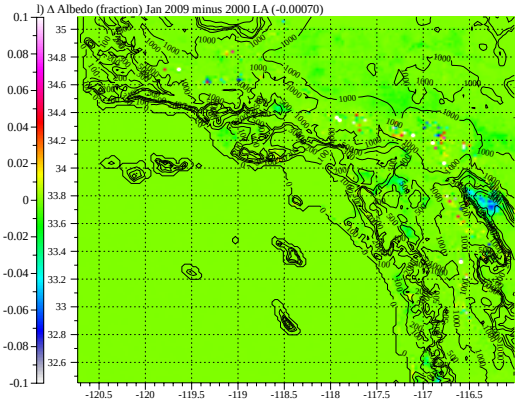


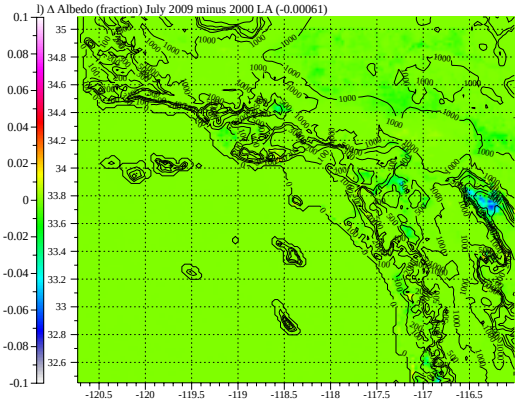

954

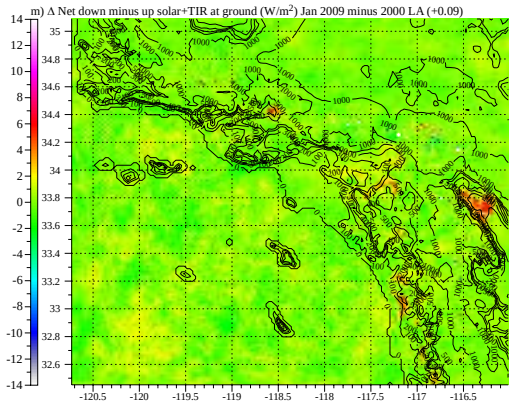


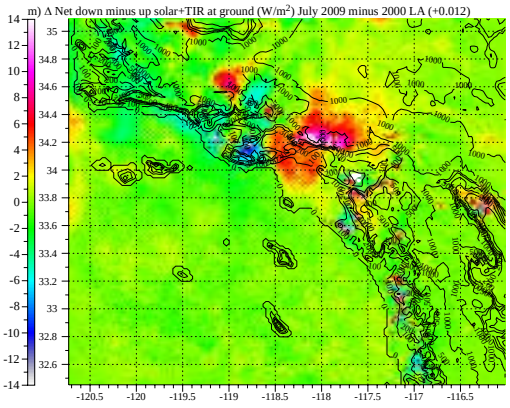


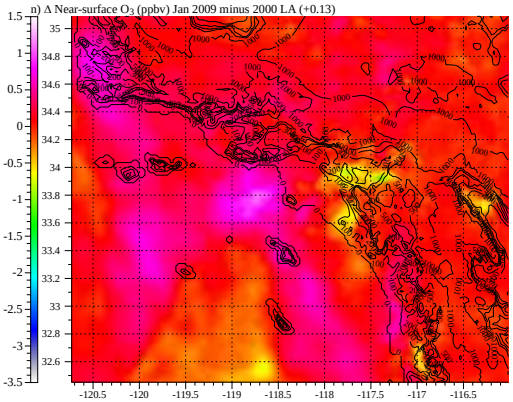


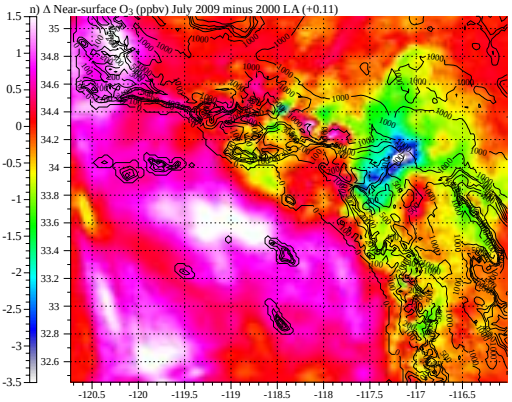


955
956
957
958
959
960

## Figure 7

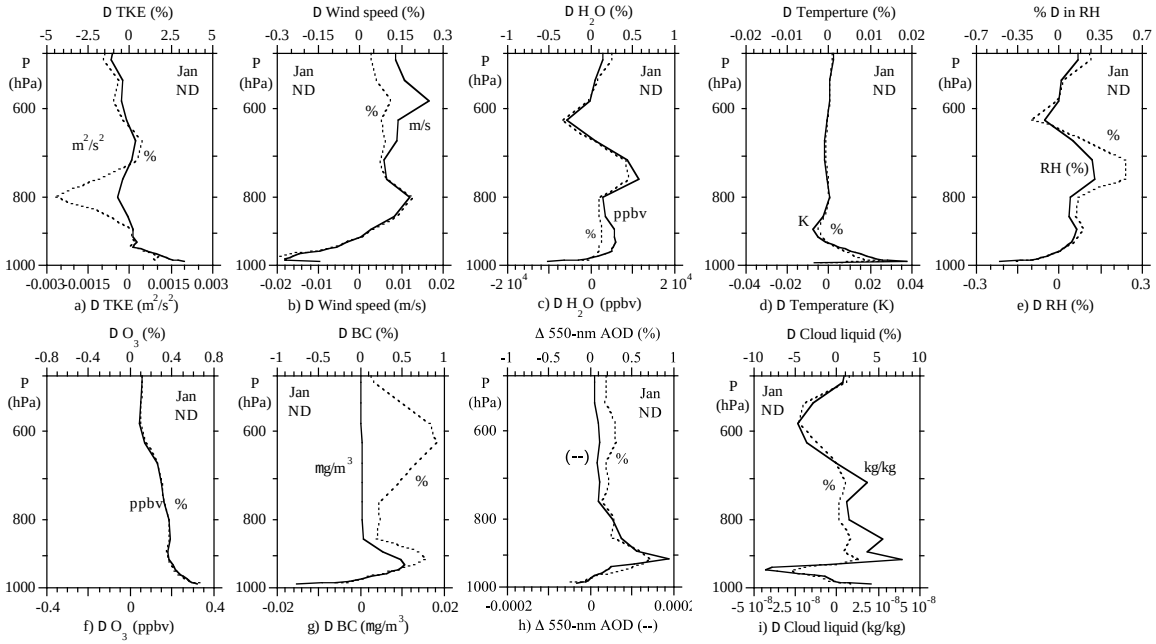


## Figure 8

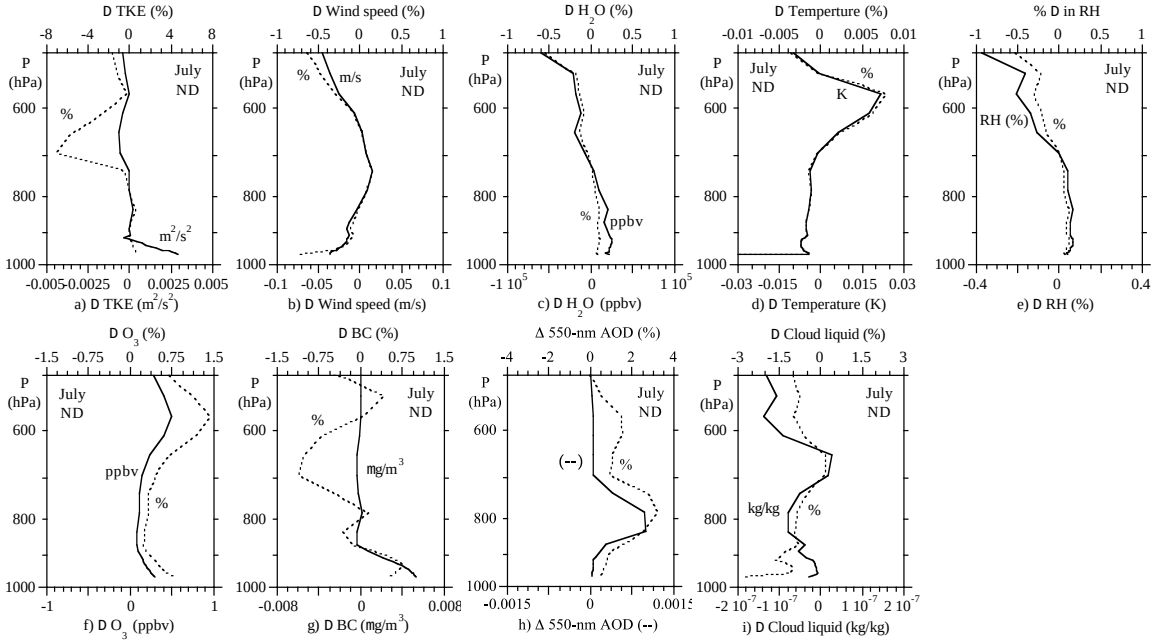

## Figure 9

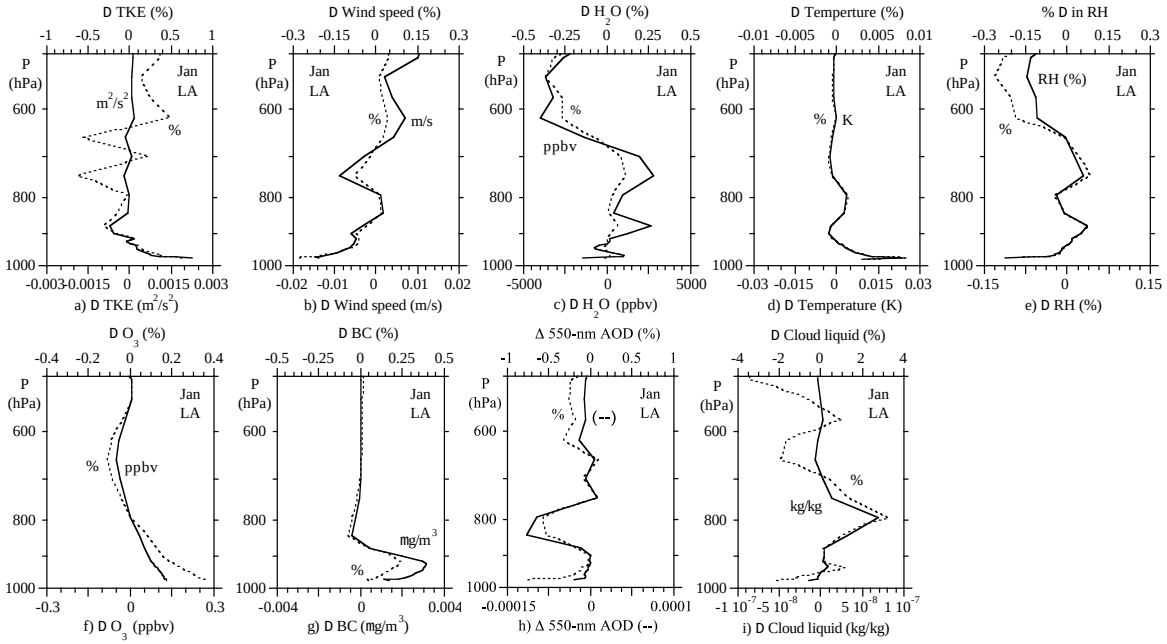


## Figure 10

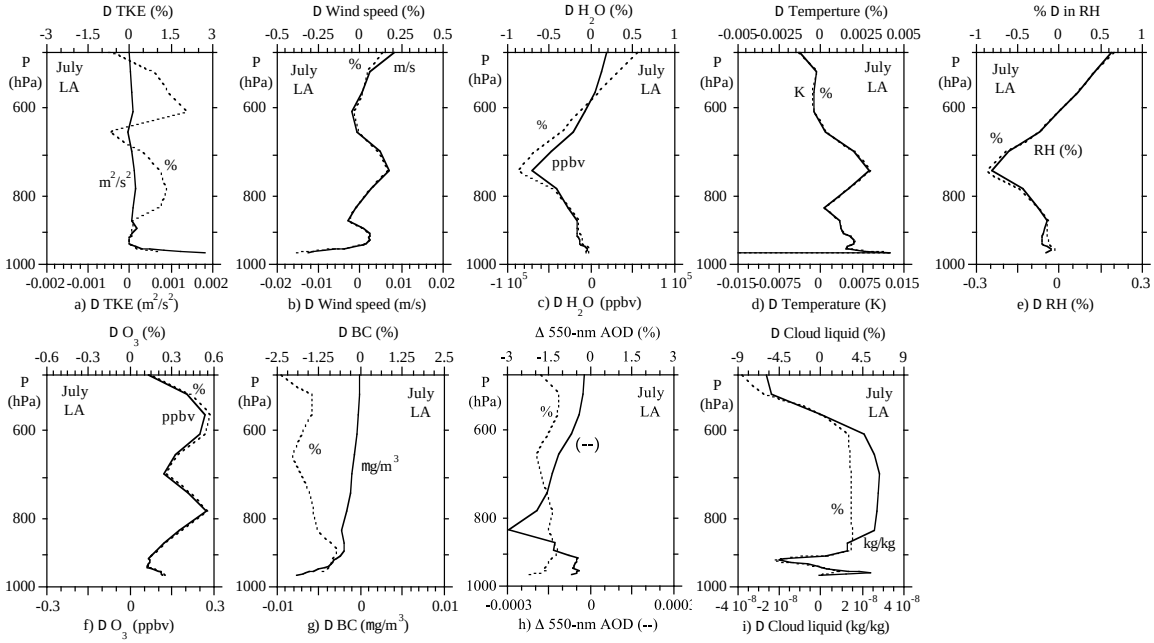

# Supplemental Information

# Short-Term Impacts of the Mega-Urbanizations of New Delhi and Los Angeles between 2000 and 2009

**Mark Z. Jacobson[1], Son V. Nghiem[2], Alessandro Sorichetta[3]**

[1]Department of Civil and Environmental Engineering, Stanford University, Stanford, California, U.S.A.

[2]Jet Propulsion Laboratory, California Institute of Technology, Pasadena, California, U.S.A.

[3]WorldPop, School of Geography and Environmental Science, University of Southampton, Southampton, U.K.

**Figure S1. S**atellite-derived (a) 2000 DSM backscatter, (b) 2009 DSM backscatter, (c) 2000 DSM backscatter index of variability (backscatter IV), and (d) 2009 DSM backscatter IV for the New Delhi model domain.

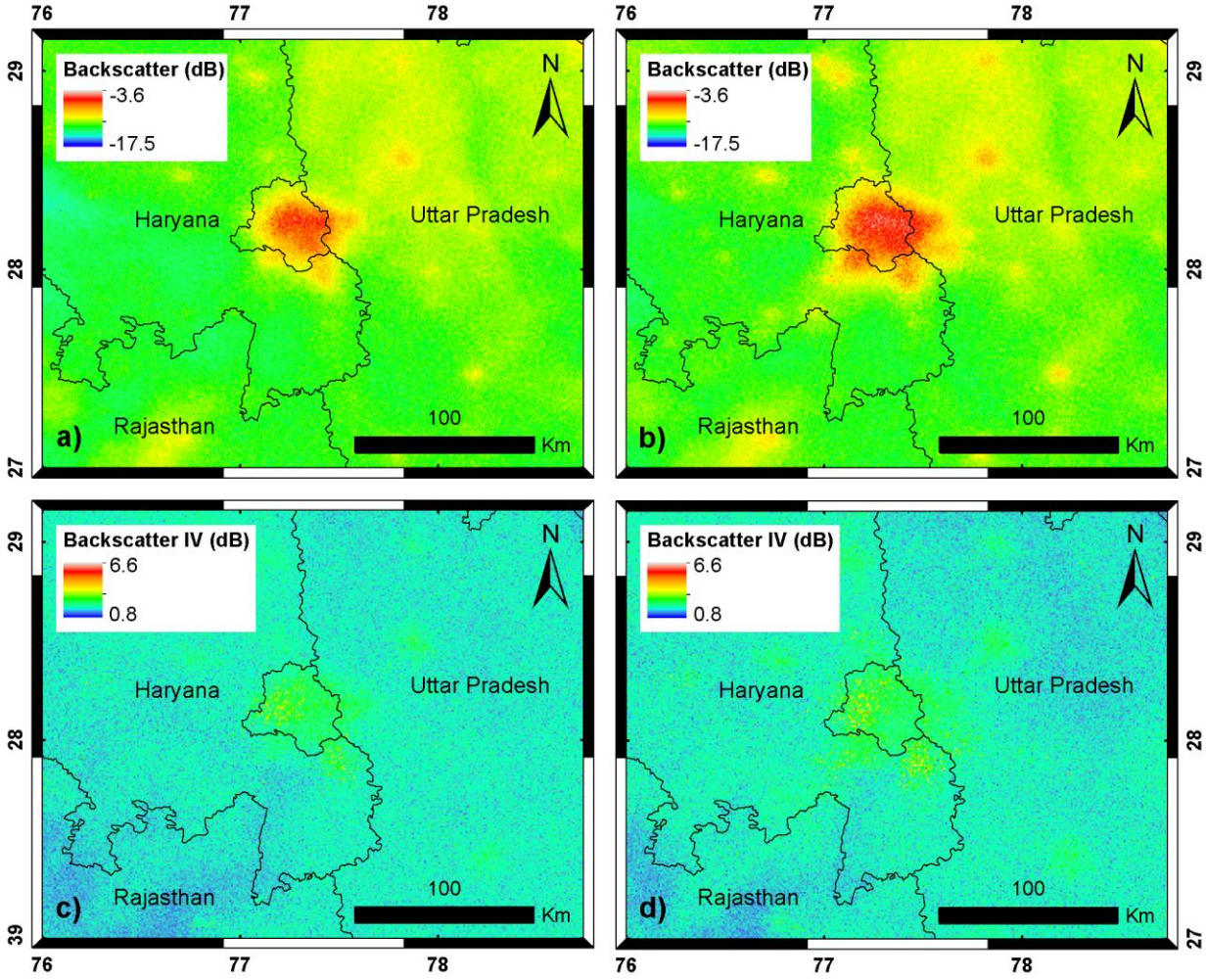

**Figure S2. S**atellite-derived (a) 2000 DSM backscatter, (b) 2009 DSM backscatter, (c) 2000 DSM backscatter index of variability (backscatter IV), and (d) 2009 DSM backscatter IV for the Los Angeles model domain. Values are shown over land only.

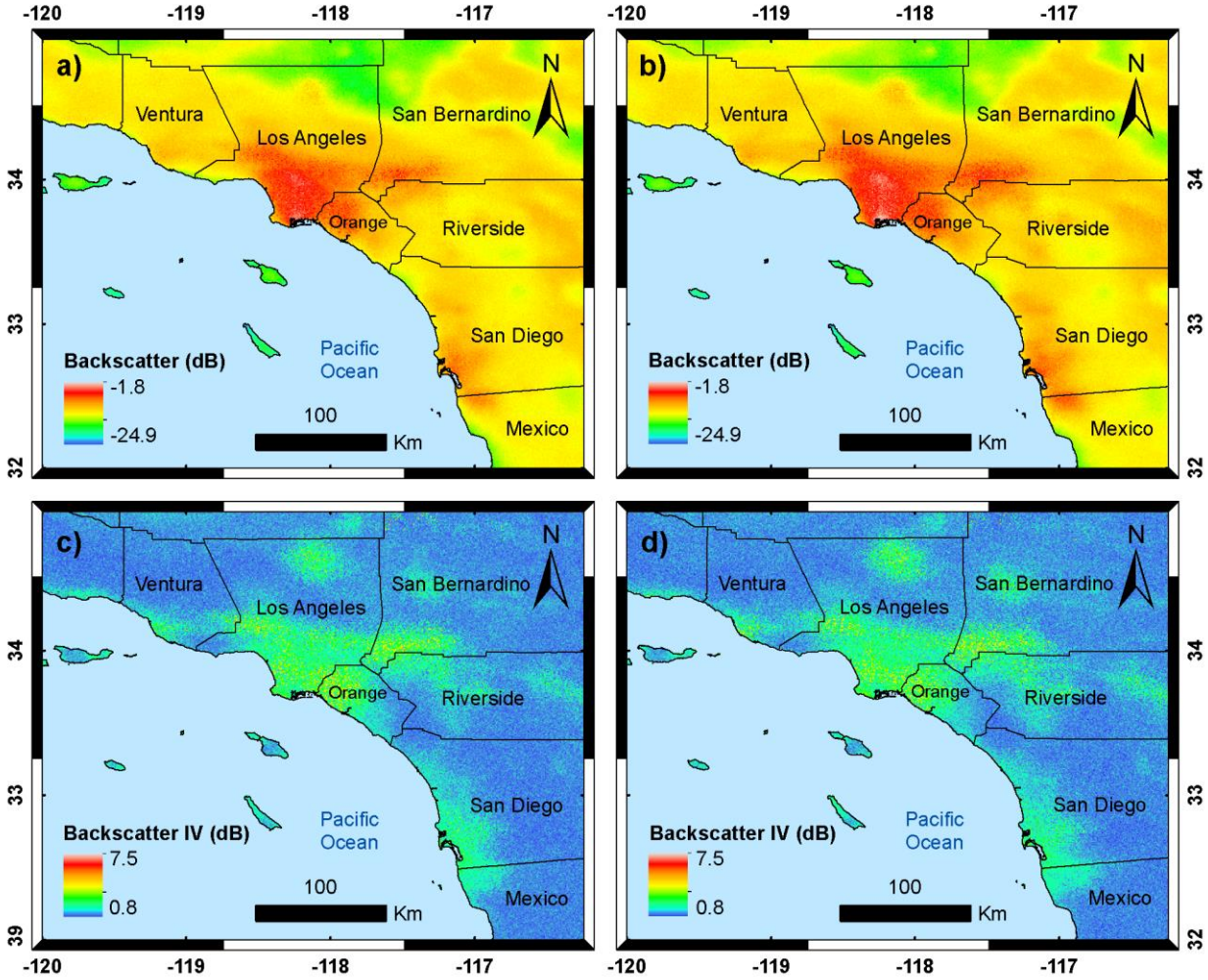

**Figure S3.** Additional comparisons (continued from Figure 4) of modeled January 2013 parameters over the India and California domains (Table 3) with *GFS* [2018] reanalysis data. The model results were from the nested simulations performed here using the 2009 urban fractions. The GFS monthly average fields (at 0.5 degree horizontal resolution) were obtained by averaging data from 32 days (January 1, 12 GMT to February 1, 12 GMT and July 1, 12 GMT to August 1, 12 GMT, 2013) and 4 times per day (00 GMT, 06 GMT, 12 GMT, and 18 GMT).

India Domain, January

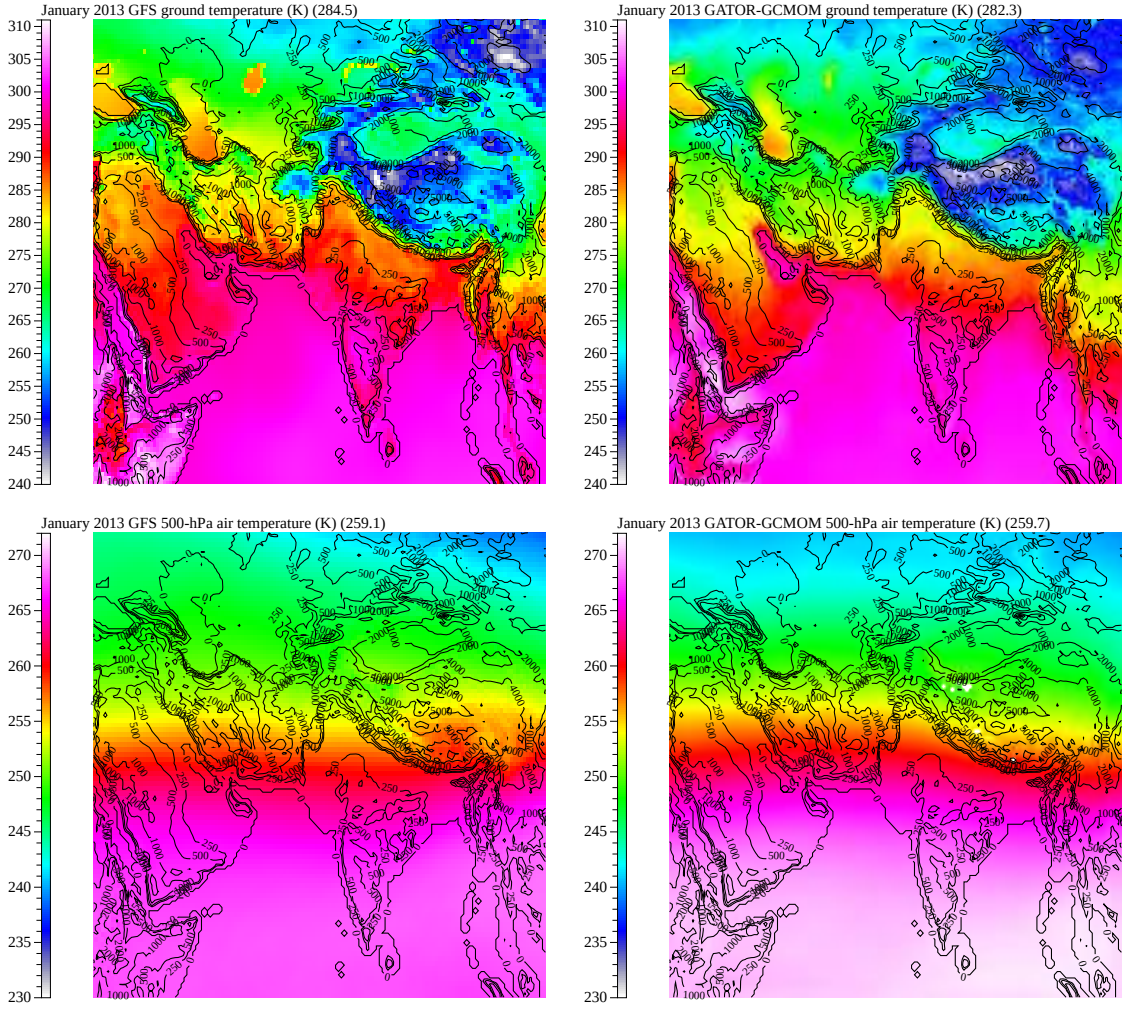

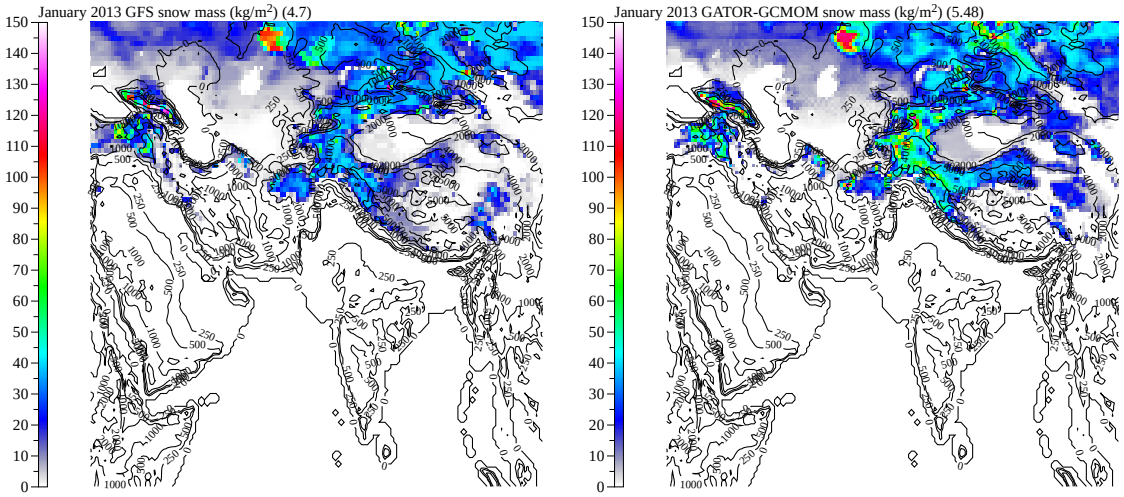


California Domain, January